Available online at www.sciencedirect.com
ScienceDirect
Journal of Nuclear Materials 374 (2008) 248–269
journal of nuclear materials
www.elsevier.com/locate/jnucmat

Evidence of Ni_2FeBO_5 and *m*-ZrO_2 precipitates in fuel rod deposits in AOA-affected high boiling duty PWR core

Jerzy A. Sawicki *

Atomic Energy of Canada Limited, Chalk River Laboratories, Chalk River, Canada ON K0J 1J0
Interatomics, University of Victoria's Vancouver Island Technology Park, Victoria, Canada BC V8Z 7X8

Received 3 April 2007; accepted 14 August 2007

Abstract

This paper describes the characteristics of corrosion product deposits found in upper regions of high axial offset anomaly (AOA) once-burnt fuel assemblies after Cycle 9 in the Callaway pressurized water reactor (PWR). The ~100-μm-thick deposits consisted of a new type of highly porous and structured Ni-, Fe-, B-, and Zr-rich material. The analyses showed that deposits contain a large amount (about 50 wt%) of Ni–Fe oxyborate (Ni_2FeBO_5, mineral name bonaccordite), in the form of matted ~0.1-μm-thick and ~10-μm-long, needle-like particles. An especially high density of Ni_2FeBO_5 needles was found in a 30–40-μm-thick zone on the clad side of the deposits. This compound has not previously been reported as a component of PWR fuel crud. Common fuel crud components such as nickel ferrite and nickel oxide were observed only in small quantities (about 10 wt%). Reference samples of Ni_2FeBO_5 were obtained by hydrothermal reactions in alkaline aqueous solutions starting from about 400 °C, or by sintering at about 1000 °C. Formation of Ni_2FeBO_5 has been identified as a new mechanism for boron retention and neutron absorption on PWR fuel. Aggregates of apparently hydrothermally precipitated ~0.1–0.3-μm-sized particles of monoclinic *m*-ZrO_2(~30 wt%) were found in the deposits, which is indicative of a dissolution–precipitation process at the cladding surface. This process may be enhanced by a LiOH concentration mechanism in crud, which is a result of both sub-cooled nucleate boiling and $^{10}B(n,\alpha)^7Li$ reactions. Consistently, the isotopic abundance of ^{10}B in Ni_2FeBO_5 in crud samples was reduced to about 10% of the total boron.

1. Introduction

The economics of power generation demand that pressurized water reactors (PWRs) are driven to higher duty cycles and longer cycle durations. As a consequence, some plants experience boiling in the upper regions of high duty cores. Among other effects, boiling duty facilitates the enhanced deposition of corrosion products (crud) on high power, mostly first load fuel rods. Such crud deposits on the fuel surfaces provide the substrate for large concentrations of boron, thereby causing the depression of thermal neutron flux via the $^{10}B(n,\alpha)^7Li$ reaction. Large amounts of boron, deposited on fuel in an axially asymmetric fashion, can give rise to the depression of thermal neutron flux in the upper part of a reactor. Such anomalous flux depressions, termed axial offset anomalies (AOAs), have been observed in increasing numbers of high-duty PWRs that use high burn-up fuel operated at high temperatures and long fuel cycles [1,2]. The affected plants typically undergo local sub-cooled nucleate boiling in the highest-power channels, which leads to an enhanced susceptibility to AOA.

Until recently, the root cause of AOA has been attributed to the hideout of lithium metaborate (γ-$LiBO_2$) in highly porous crud deposits [3,4]. However, this compound has retrograde solubility and has never been directly observed in PWR fuel deposits. Plant-to-plant and cycle-to-cycle variations in the extent of AOA also suggest that other factors are involved in the root cause, including characteristics of crud sources, reactor coolant system (RCS) chemistry, and especially nickel, iron, boron and lithium concentrations. Thus, too little is known about the nature

* Address: Interatomics, University of Victoria's Vancouver Island Technology Park, Victoria, Canada BC V8Z 7X8. Tel.: +1 250 220 6923.
E-mail address: jasawicki@shaw.ca

0022-3115/$ - see front matter © 2007 Elsevier B.V. All rights reserved.
doi:10.1016/j.jnucmat.2007.08.014

of these deposits and the mechanism of their deposition to fully understand the root cause of AOA.

The objective of this work was to determine the properties of fuel corrosion products from Callaway Cycle 9 as they relate to the severe AOA observed for this core. Analyses have demonstrated that the deposits at this high-duty plant are qualitatively, as well as quantitatively, different from deposits in lower duty (non-boiling) PWRs. In particular, large amounts of Ni_2FeBO_5 and *m*-ZrO_2 were found in the Callaway deposits, while common components of fuel crud deposits such as nickel ferrite and nickel oxide were observed only in minor quantities. Unexpected preliminary results of this work [1,5,6] have triggered considerable discussion and modeling efforts [7–9] in order to better describe the nuclear, chemical and hydrothermal phenomena in borated fuel crud and thus to validate the root cause of axial offset anomaly in high-duty PWR cores.

2. Characteristics of reactor core and samples

2.1. Reactor core

The AmerenUE 3565 MW(th) Callaway plant is a 4-loop Westinghouse PWR reactor with Model F, Inconel 600 Mill Annealed alloy steam generators having a total tube surface area of 29 440 m^2. The Cycle 9 core consisted of 193 Vantage five fuel assemblies, each with a 17×17 matrix of 9.1-mm diameter pins. The ratio of steam generator to fuel surface area is 3.82. The water volume in the core is about 18.8 m^3. The volume of the reactor cooling system is 322.6 m^3, including the pressurizer. At full power, the mass of water is 2.38×10^5 kg, the pressure is 15.4 MPa, the flow rate is 25 m^3/s, and the bypass flow is 4.8%.

AOA has been observed for several Callaway fuel cycles, beginning with Cycle 4. During Cycle 9, from November 13, 1996 to April 9, 1998, after seven months of operation at full power, AOA reached the −14% level, the highest observed at any plant until that time. Table 1 lists the core and chemistry parameters for Cycle 9 and the fuel cycles immediately preceding and following. Since such severe AOA reduces the shutdown margin by shifting power towards the bottom of the core, during the remainder of Cycle 9 the reactor had to be de-rated to 70% full power. In Cycle 10, the core design was less aggressive (less steaming) than in Cycle 9, and additional wet annular burnable absorbers were used. Still, Cycle 10 showed the onset of AOA on the reload fuel from the beginning of the cycle, presumably because a number of the Cycle 9 feed fuel assemblies, having a large amount of deposit, were reloaded into high-power locations for Cycle 10. AOA was also observed in Cycle 11.

Table 1
Comparison of reactor core and chemistry parameters in Callaway fuel Cycles 8, 9, and 10

	Cycle 8	Cycle 9	Cycle 10
Core parameters			
Cycle length (*d*)	530	508	517
Cycle length EFPD[a](*d*)	495	436	495
T_{avg} (°C)	308.9	308.5	308.5/306.4
T_{hot} (°C)	325.5	325.5	325.5/323.3
T_{cold} (°C)	292.3	291.8	291.8
Number of IFBAs[b]	6272	7712	6880
Number of WABAs[c]	0	0	544
AOA (%)	−8	−14	−12
Chemistry			
Max. boron (ppm)	1400	1380	1230
Max. lithium (ppm)	2.2	2.6	2.9
pH at T_{avg}	6.95–7.4	7.0–7.1	7.1–6.9–7.2
Average ^{58}Co (Bq/g)	141	592	777
Refueling ^{58}Co return (TBq)	40.6	37.1	72.0
Refueling Ni return (kg)	4.2	3.3	4.1

[a] EFPD (effective full power days).
[b] IFBAs (integral fuel burnable absorbers). These fuel pellets have a coating of zirconium diboride. This burnable poison is consumed within about 3 to 4 months.
[c] WABAs (wet annular burnable absorbers). These absorbers suppress power for a much longer time during the cycle than IFBA rods.

2.2. Characteristics of the samples

In common with other PWRs exhibiting AOA, Callaway Cycle 9 showed Fe–Ni oxide deposits on fuel rods near the top of the core. The deposits were especially thick (about 100 μm) in Spans 5a, 5b, 6a and 6b, the regions of intense sub-cooled nucleate boiling on high-duty feed (first cycle) fuel assemblies. Two fuel rod crud scrapes were examined in this work. These are henceforth identified as scrapes #1 and #2, and were taken on April 16, 1998 from span 6a of high-power feed fuel assemblies L22 and L31, respectively. These assemblies had been in service for about 18 months, accumulating 25.5 and 22.8 GWd/tU burn-up, respectively. The power parameters for assemblies L22 and L31 are listed in Table 2. The end of cycle (EOC) rod power calculated to account for the observed AOA and the predicted assembly power without AOA, are shown in the last two columns of Table 2. The clad temperature of these assemblies was estimated to be about 348 °C.

The samples were obtained using an established Westinghouse scraping technique [10,11] by taking 30-cm-long scrapes along fuel rod surface. The dislodged crud was collected by drawing the spent fuel pool water containing the deposit suspension into a polyethylene sample bottle by

Table 2
Local power characteristics of sampled fuel assemblies at the end of Cycle-9

Sample	Assembly	Relative power at EOC	Burnup at EOC (GWd/tU)	AOA (%)	Rod/assembly power ratio	Assembly/average core power ratio
#1	L22	1.170	22.844	−14.1	1.286	1.16
#2	L31	1.309	25.555	−18.3	1.304	1.34

means of a vacuum system, followed by filtration through a 0.45-μm-pore-size 47-mm diameter Millipore filter membrane. The filter cake of collected solids was then washed twice with 100 mL of de-ionized water to remove any soluble material.

3. Analyses

3.1. Radionuclides

The filter packages received by AECL contained a 30-mm-diameter, brown-coloured ~10-μm-thick crud cake and numerous fragile ~0.05 to 0.12-μm-thick and ~1 to 3-mm-sized flakes, either loose or loosely attached to the filter surface. The flakes were very fragile and broke easily if touched gently. Radiation surveys indicated contact dose rates of about 5 R/h gamma and about 5 R/h beta. The total gamma activity on January 30, 1999 was 0.6 mCi for sample #1 and 1.5 mCi for sample #2. Specific activities were determined using a small portion of the solution obtained by dissolving 2.6 mg of sample #1 crud flakes in a 50 mL volume of solvent. The sample analyzed was that used for the quantitative chemical analysis (see Table 6). The gamma spectroscopy analysis and weight data showed the specific activity of ^{60}Co on 1997 April 16 to be about 14 mCi/g. The count rate of α-particles was 40 000–50 000 counts/min per filter; the specific α-activity of crud was determined to be about 1.4 μCi/g.

Small fragments of the filter paper and some loose flakes were analyzed using a calibrated gamma spectrometer with a high-purity coaxial germanium detector. The gamma-emitting radioactive isotopes identified in the samples, and their respective activities on June 11, 1999, are listed in Table 3. The main radioisotopes found were activated corrosion products through the reactions ^{54}Fe(n,p)^{54}Mn, ^{58}Ni(n,p)^{58}Co, ^{59}Co(n,γ)^{60}Co, ^{94}Zr(n, γ)^{95}Zr(β$^-$)^{95}Nb, and ^{124}Sb(n,γ)^{125}Sb. The ^{58}Co isotope is a dominant source of radioactivity in Ni-rich fuel crud samples, and the high ^{58}Co/^{60}Co ratio is an indicator of a high Ni/Co ratio. Decay correction of data in Table 3 to the end of Cycle 9 indicates that the ^{58}Co/^{60}Co ratios for the sample #1 filter cake and flakes are 32.9 and 23.7, respectively. The respective ratios for the sample #2 filter cake and flakes 1 and 2 removed from #2 sample are 34.4, 24.0, and 22.4, respectively. Thus, the filter cake samples have consistently higher initial ^{58}Co/^{60}Co ratios (33–34) than the loose flakes (22–24). This may suggest that during exposure to neutrons the average Ni/Co ratio was lower in the crud flakes than in the fine particles collected in the filter cake, or that the exposure time of the crud flakes was longer than the exposure time of material collected in the filter cake.

The X-ray and γ-emitters in the energy range below 80 keV cannot be detected by conventional general-purpose gamma spectrometers, such as the one used for the measurements discussed above. A good definition of low-energy activities was needed for developing the best procedures for further work, particularly for X-ray fluorescence (XRF), Mössbauer spectroscopy, and electron microscopy. The low-energy γ-rays and X-rays were measured with a liquid-nitrogen-cooled intrinsic planar 1-cm-thick germanium detector equipped with a very thin beryllium window. The low-energy part of the spectra were dominated by overlapping X-ray lines of 5.4 keV CrK$_\alpha$ from ε decay of ^{54}Mn, 5.9 keV MnK$_\alpha$ from ε decay of ^{55}Fe, 6.4 keV FeK$_\alpha$ from ε decay of ^{58}Co and 6.9 keV CoK$_\alpha$ from β$^-$-decay of ^{60}Co. In the middle of the spectra, one finds 15.8 keV ZrK$_\alpha$ and 17.7 keV ZrK$_\beta$ lines from Zr XRF of the sample, 16.6 keV NbK$_\alpha$ and 18.7 keV NbK$_\beta$ lines from β$^-$-decay of ^{95}Zr, as well as a 23.9 keV peak ascribed to gamma rays from $^{119\,m}$Sn. At higher energies, one finds lines of 27.5 keV TeK$_\alpha$ and 31.0 keV TeK$_\beta$ from β$^-$-decay of ^{125}Sb, 25.3 keV SnK$_\alpha$ and 28.5 keV SnK$_\beta$ lines from electron conversion in ^{119m}Sn, and the 35.5 keV gamma-ray line of ^{125}Te from β$^-$-decay of ^{125}Sb.

The XRF provided the first evidence of an unexpectedly large content of zirconium in the samples. The XRF spectra of crud samples were obtained using a 20 mCi ^{109}Cd excitation source emitting 22.1 keV and 24.9 keV AgK X-rays and a liquid-nitrogen-cooled Li-drifted silicon detector. The best-resolved and distinct lines in the XRF spectra were 7.5 keV NiK$_\alpha$ and 8.3 keV NiK$_\beta$ lines, and 15.8 keV ZrK$_\alpha$ and 17.7 keV ZrK$_\beta$ lines. X-ray emission spectra showed overlapping X-ray lines from ε decays of ^{54}Mn (5.4 keV CrK$_\alpha$), ^{55}Fe (5.9 keV MnK$_\alpha$) and ^{58}Co (6.4 keV FeK$_\alpha$), as well as a 6.9 keV CoK$_\alpha$ line from β$^-$-decay of ^{60}Co. Because of the strong interference of X-rays from the specimen's own radioactivity, the concentration of Fe

Table 3
Gamma activities of small fragments of crud samples referenced to June 11, 1999

Isotope	Half-life	#1 cake (%)	#1 flake (%)	#2 cake (%)	#2 flake 1 (%)	#2 flake 2 (%)
^{54}Mn	312.2 d	15.4	16.0	17.9	15.0	15.3
^{57}Co	271.8 d	1.4	1.1	1.0	1.2	1.1
^{58}Co	70.9 d	30.4	24.3	27.9	24.7	23.4
^{60}Co	5.27 y	49.1	53.8	42.8	54.5	55.1
^{65}Zn	243.8 d	–	–	0.3	0.2	0.2
^{95}Zr	64.0 d	1.0	1.5	2.0	0.6	0.7
^{95}Nb	35.0 d	–	0.7	4.5	1.5	1.8
^{113}Sn	115.1 d	0.7	0.7	0.9	0.6	0.5
^{125}Sb	2.76 y	2.0	2.0	2.9	1.7	1.8
Total (×10^5 Bq)		0.7	1.4	0.5	1.9	2.4

could not be determined from the intensity of the unresolved 6.4 keV FeK$_\alpha$ line in the XRF spectra.

3.2. Mössbauer spectroscopy

Mössbauer absorption spectra of the 14.4-keV ^{57}Fe γ-rays were obtained to determine the phase composition of iron-bearing compounds in the crud samples. This is the first instance in which Mössbauer spectroscopy has been successfully applied to crud samples from nuclear reactor fuel. In general, Mössbauer spectroscopy of fuel crud samples is difficult, because (i) the samples' alpha, beta and gamma radioactivity produces high radiation fields; (ii) the iron concentration is small compared with nickel and zirconium; and (iii) the fragile samples are difficult to handle for the preparation of absorbers of suitable form, uniform density, and homogeneity.

Mössbauer absorbers were prepared from either 50% of the filter cake or about 3 mg of the loose debris. The samples were encapsulated in thin gamma-transparent plastic containers, without pressing or damaging the flakes, and without using any filling material or glues. The analyses were carried out with an Amersham 50-mCi single-line Mössbauer source of ^{57}Co in a 6-μm rhodium matrix. The velocity scale of the spectrometer was calibrated using a 25-μm-thick α-Fe absorber. All spectra were recorded at room temperature using a Reuter–Stokes Kr–CO_2 proportional counter and a Halder–Canberra Mössbauer spectrometer.

The Mössbauer absorption spectra of ^{57}Fe in the crud samples are presented in Fig. 1. Each spectrum was recorded for 45 days to acquire adequate counting statistics. The spectra were interpreted as the superposition of hyperfine sextuplets and doublets of Lorentzian-shaped absorption lines. The numerical results of the least-squares analyses listed in Table 4 include the determination of δ_{Fe}, the centroid shift relative to that of α-Fe at 295 K; ΔE_Q, the quadrupole splitting at the iron sites; Γ, the line-width for the Lorentzian distributions; H, the hyperfine magnetic field at the iron sites; and A/B, the area ratio of spectral components from iron at A- and B-sites in the spinel-type matrix. The total spectrum areas (in arbitrary units) and the fractional areas under individual spectrum components (as a percent of the total spectrum area) are also listed. The numbers in parentheses are the one-sigma statistical errors of the last significant digit. The numbers given without errors were fixed during the fitting procedure.

The spectrum component consisting of two overlapping sextuplets could be readily ascribed to nickel ferrite, $NiFe_2O_4$. However, the central quadrupole-split doublet did not have an immediately available interpretation. This unknown doublet dominated the spectra of filter flakes, while its intensity was considerably smaller in the spectra of the filter cake. The centroid shift value, $\delta_{Fe} = 0.37$ mm/s, for this component was typical of octahedrally coordinated Fe^{3+} ions, although the corresponding magnitude of the electric quadrupole splitting $\Delta E_Q \sim 1.2$ mm/s appeared to be rather large for common ferric oxides with octahedrally coordinated Fe^{3+} ions.

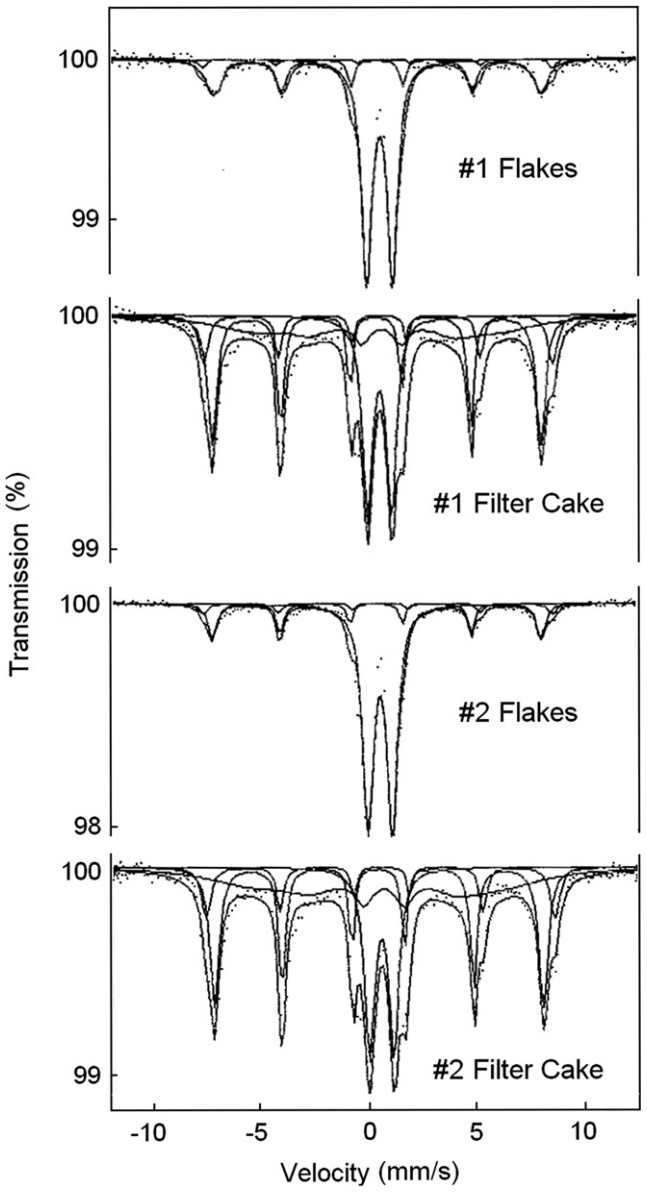

Fig. 1. ^{57}Fe Mössbauer transmission spectra obtained at room temperature of fuel crud samples in the form of flakes and filter cake.

In an attempt to identify this unknown component, various possibilities within the set of Fe and Fe/Ni-oxides and oxyhydroxides systems, metallic alloy phases, phases such as an 'Fe in NiO' solution phase, or very small nickel ferrite particles were considered, but none gave an acceptable spectrum match. The possibility that the unknown doublet represented an iron borate was considered, but the literature review uncovered no iron borates with the appropriate spectral parameters. A better match was found with the iron-nickel borates. Published δ_{Fe} and ΔE_Q Mössbauer parameters of one of the boro-ferrites in the ludwigite–vonsenite series [12–16], known as the mineral bonaccor-

Table 4
Results of ^{57}Fe Mössbauer spectroscopy analyses of fuel crud samples and some reference specimens

Sample	Phase/site	Total area	Rel. area (%)	δ_{Fe} (mm/s)	ΔE_Q mm/s)	H (Tesla)	W (mm/s)	Fraction (wt%)
Crud samples								
#1 flakes	Ni_2FeBO_5	0.024	67(2)	0.37	1.17	–	0.56(1)	85.9
	$NiFe_2O_4$ (A)		25(2)	0.23	0.04	49.2	0.53	14.1
	(B)		8(2)	0.37	−0.06	52.2	0.54	
#1 cake	Ni_2FeBO_5	0.029	27(2)	0.37	1.17	–	0.57	65.8
	$NiFe_2O_4$ (A)		33(1)	0.23	0.04	49.2	0.53	20.3
	(B)		12(2)	0.37	−0.06	52.2	0.54	
	α-FeOOH		28(1)	0.37	−0.27	37.5	4.3(5)	13.9
#2 flakes	Ni_2FeBO_5	0.032	73(1)	0.37	1.17	–	0.57(1)	86.5
	$NiFe_2O_4$ (A)		21(1)	0.23	0.04	49.2	0.53	13.5
	(B)		6(1)	0.37	−0.06	52.2	0.54	
#2 cake	Ni_2FeBO_5	0.046	22(1)	0.37	1.17	–	0.57	71.7
	$NiFe_2O_4$ (A)		32(1)	0.23	0.04	49.2	0.53	17.2
	(B)		12(1)	0.37	−0.06	52.2	0.54	
	α-FeOOH		34(1)	0.37	−0.27	37.0	5.7(5)	11.1
Reference data								
This work	Ni_2FeBO_5	0.172	100	0.36(1)	1.17(1)	–	0.52(1)	
Ref. [18]			100	0.36	1.20	–	–	
Ref. [19]	Site 1	–	10	0.29	1.08	–	0.26	
	Site 2	–	30	0.34	1.28	–	0.33	
	Site 3	–	54	0.38	1.08	–	0.31	
	Site 4	–	6	0.35	1.93	–	0.36	
This work	$NiFe_2O_4$ (A)	0.272	44(2)	0.23(1)	0.04(1)	49.2(4)	0.53(1)	
	(B)		56(2)	0.37(1)	−0.06(1)	52.2(3)	0.54(1)	
Ref. [20]	$NiFe_2O_4$ (A)	–	50	0.26(3)	0.00(3)	49.7(5)	0.5	
	(B)		50	0.36(3)	0.00(3)	52.6(5)		
This work	α-FeOOH	–	100	0.37(3)	−0.27(3)	38.2(5)	1.00	

δ_{Fe} is the isomer shift with respect to ^{57}Fe in an α-Fe absorber, ΔE_Q is the electric quadrupole splitting, and W is the full linewidth at half maximum. Last digit(s) errors are given in parentheses.

dite (formula Ni_2FeBO_5) [17], matched the doublet parameters measured on the Callaway crud surprisingly well.

The four Mössbauer spectra of Callaway crud samples were fit to library spectra of Ni_2FeBO_5, $NiFe_2O_4$ sites A and B, and α-FeOOH by adjusting the relative quantities of these components to provide the best fit with the spectra of the crud samples. To obtain the final fit, the parameters derived from reference spectra of synthetic Ni_2FeBO_5 and $NiFe_2O_4$ were used. Table 4 lists the results of this analysis, together with the measured parameters of reference specimens.

Reference samples of $NiFe_2O_4$ and Ni_2FeBO_5 were prepared from simple oxides or oxy-hydroxides by both dry (sintering in air) and wet (hydrothermal reaction and crystallization) methods. In the dry synthesis, stoichiometric mixtures of NiO and Fe_2O_3 (for $NiFe_2O_4$), and NiO, Fe_2O_3 and H_3BO_3 (for Ni_2FeBO_5) were calcinated at 500 °C for 24 h, ground to a powder, and sintered for 24 h at 900 °C and 1000 °C in air. Nickel ferrite was also produced from slurry of NiO and Fe_2O_3 at temperatures of about 300 °C. Ni_2FeBO_5 was fabricated at temperatures starting from 400 °C from slurry of NiO, Fe_2O_3, and H_3BO_3, with the addition of LiOH to create a sufficiently alkaline environment. The particles of Ni_2FeBO_5 produced by hydrothermal reactions had a similar morphology as the needles observed in the reactor crud.

The Mössbauer spectra of the synthetic $NiFe_2O_4$ and Ni_2FeBO_5, as well as that of two reference mixtures of these compounds in 1:1 and 1:4 weight ratios, are presented in Fig. 2. The spectra of the mixed compounds clearly match the corresponding spectra of the crud samples shown in Fig. 1. The parameters of the Mössbauer spectra are listed in Table 4.

Determining weight fractions of the identified iron compounds from their relative spectral areas requires some assumptions to be made about the values of the Lamb–Mössbauer factors f_a for Ni_2FeBO_5, $NiFe_2O_4$, and α-FeOOH. The value of f_a for Ni_2FeBO_5 has not been measured; thus, it was simply assumed that the f_a factors for all three compounds are equal. The results are summarized in the last column of Table 4.

The following is a brief discussion of the properties of Ni_2FeBO_5 and $NiFe_2O_4$ found in the fuel crud samples studied in this work.

Compounds of the general formula M_2FeBO_5 (where M = Fe, Ni, or Cu) were first synthesized by dissolution of M_2O_3 in an alkaline boric medium, followed by slow cooling [12,13]. These anhydrous oxyborates have the general chemical formula $M(II)_2M(III)O_2(BO_3)$; where $M(II) = Mg^{2+}$, Fe^{2+}, Co^{2+}, Ni^{2+}, Cu^{2+}, etc., and $M(III) = Al^{3+}$, Ti^{3+}, Cr^{3+}, Mn^{3+}, Fe^{3+}, Co^{3+}, Ga^{3+}, etc. These compounds have the same structure as the mineral ludwigite (Mg_2FeBO_5), which has an orthorhombic-bipyramidal unit cell (space group V_h^9-*Pbam*) (13-16]. In the ludwigite structure, MO_6 octahedra share edges, giving rise to zig-zag walls that are parallel to a short crystallographic

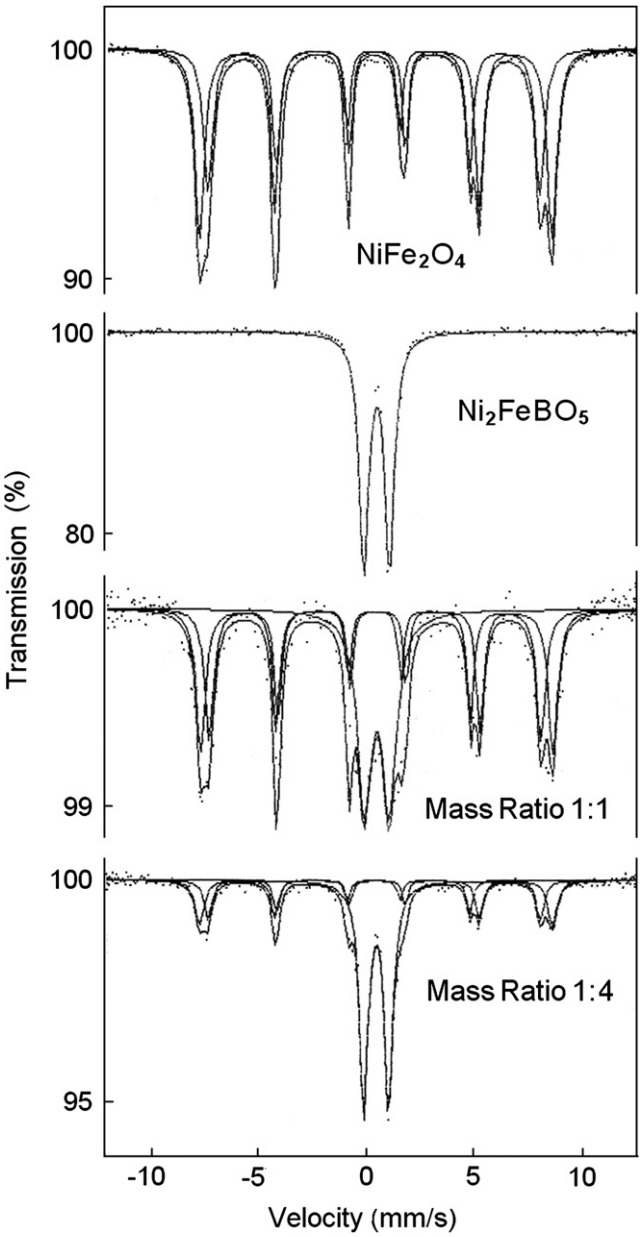

Fig. 2. ^{57}Fe Mössbauer transmission spectra obtained at room temperature of synthetic $NiFe_2O_4$ and Ni_2FeBO_5, and two samples of $NiFe_2O_4$ and Ni_2FeBO_5 mixed in 1:1 and 1:4 weight ratios.

c-axis of length ~0.3 nm, equal to the intra-chain metal–metal distance. The boron ions remain at the centers of planar-trigonal borate groups, BO_3^{3-}, which is the strongest bonded group of ions in the structure. The simplified crystal structure of bonaccordite is shown in Fig. 3. Note that the covalent bonds between boron and oxygen in these groups are among the strongest known chemical bonds.

Like the other minerals of the ludwigite type, Ni_2FeBO_5 crystallizes in the form of slender long rods with acicular habits ('needles'). Typical of an anhydrous borate, it is insoluble in water and is only very slightly soluble in common mineral acids. It has high density (5.17 g/cm^3) and high hardness (7 in Mohs units), similar to quartz. It is a

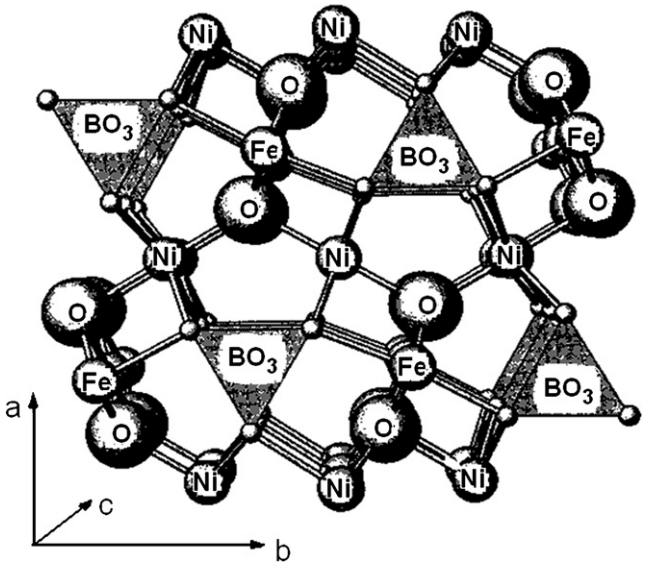

Fig. 3. Simplified crystal structure of bonaccordite N_2FeBO_5.

one-dimensional magnetic and electronic material–paramagnetic at room temperature and antiferromagnetic below 51 K.

Mössbauer spectra of Ni_2FeBO_5 samples of mineralogical origin have not been reported to date. The room temperature Mössbauer spectrum of synthetic Ni_2FeBO_5 [18] represents a doublet of broad absorption lines, with a centroid shift of $\delta_{Fe} = 0.36$ mm/s and a quadrupole splitting of $\Delta E_Q = 1.20$ mm/s (see Table 4). Recent Mössbauer studies by Fernandes et al. [19] indicate that Fe^{3+} ions are distributed in Ni_2FeBO_5 over four non-equivalent crystallographic sites, each described by different values of δ_{Fe} and ΔE_Q, and different site populations A (see Table 4). However, since the population of sites 1 and 4 is relatively small, the Mössbauer spectra of Ni_2FeBO_5 can be fairly well approximated by a superposition of two quadrupole doublets at sites 3 and 2, or even one doublet of two broadened absorption lines, as was assumed by Abe et al. [18]. The single-doublet approximation was used in this work. The parameters of the central doublet in the spectra of crud samples ($\delta_{Fe} = 0.37$ mm/s and $\Delta E_Q = 1.18$–1.26 mm/s, see Table 4) were derived from least-squares analysis, and agreed well with averaged values of the corresponding parameters reported in the literature for synthetic Ni_2FeBO_5, as well as with the values of these parameters obtained by us for synthetic samples.

The mineral trevorite, a stoichiometric nickel ferrite, is an inverse spinel, in which the tetrahedral A-sites are occupied by Fe^{3+} ions and the octahedral B-sites by Fe^{3+} and Ni^{2+} ions. The general formula of stoichiometric nickel ferrite can be written as (Ni)[Ni,Fe]O_4; where the round and square brackets represent A- and B-sites, respectively. The magnetic structure is generally assumed to be the Néel collinear type, that is, the magnetization of the A-sublattice is anti-parallel to that of the B-sublattice. The room temperature Mössbauer spectrum of nickel ferrite exhibits

two overlapping six-line hyperfine patterns corresponding to ^{57}Fe in A- and B-sites [20] (see Table 4).

In the Mössbauer spectra of fuel crud samples, the outermost B-lines of $NiFe_2O_4$ are considerably broader and less intense than the corresponding A-lines, whereas the second and fifth lines are unresolved (see Fig. 1) and cannot be separated into A- and B-site components. This type of effect in the Mössbauer spectrum of $NiFe_2O_4$ can be attributed to either non-stoichiometry [20] or very small particle size [21,22]. In the present case, non-stoichiometry is likely caused by chromium ions. Chemical analysis of sample #1 crud cake and flakes (see Table 6) yielded Cr/Fe weight ratios of 0.11 and 0.03, respectively. Chromium ions would preferentially occupy the octahedral B-sites in a mixed nickel–chromium–iron ferrite of the general formula $(Ni_{1-X}Fe_X)[Ni_XFe_{2-X-Z}Cr_Z]O_4$; where X, the inversion parameter, can be as high as 1. It was shown [23] that for Z as low as 0.05, the intensity of the outer lines in the Mössbauer spectrum is notably reduced compared with the spectrum of pure $NiFe_2O_4$. Because much of the iron in the crud is consumed by the formation of Ni_2FeBO_5, the resultant Cr/Fe ratio in the nickel ferrite found in the crud may be even higher than 0.1. At that weight ratio, the Mössbauer spectrum would exhibit only a single unresolved sextuplet of lines with notably reduced magnetic hyperfine splitting. This fairly accurately describes the pattern observed for nickel ferrite in the crud samples.

The notable broadening of $NiFe_2O_4$ lines in the crud samples can be ascribed to both non-stoichiometry and the small size of the observed particles. A study of Mössbauer spectra of nickel ferrite particles with compositions close to $Ni_{0.9}Fe_{2.1}O_4$ and particle sizes in the range of 25–130 nm revealed that the smallest particles in this range exhibited line broadening and a slightly reduced hyperfine field [21]. The effect has been related to a collective excitation mechanism. According to this mechanism, thermally excited oscillations of the magnetization around an energy minimum below the super-paramagnetic blocking temperature reduce the magnetic hyperfine splitting in the Mössbauer spectrum, resulting in asymmetrically broadened lines.

In the Mössbauer spectra of fuel crud samples there appears a third, rather poorly defined component. This component has been ascribed to goethite α-FeOOH, which is a common phase in corrosion products formed in moist air or oxygenated water. Goethite is antiferromagnetic below the Néel temperature, $T_N \approx 393$ K. The Mössbauer spectra of stoichiometric and well-crystallized goethite exhibit, at room temperature, a sextet of absorption lines described by the parameters listed in Table 4. Mössbauer spectra of colloidal goethite in corrosion products often show a considerable broadening of the lines, or show a characteristically asymmetric pattern of six wide overlapping lines. Such a spectral shape has been explained by super-ferromagnetism, that is, magnetic coupling among goethite crystallites in the size range of 0.1 μm or less [24,25].

The goethite parameters identified in both filter cake samples suggest that this material may also occur in the form of very small crystallites. X-ray diffraction patterns of such fine particles may not be well characterized. Since goethite is unstable at reactor core temperatures at power, its presence in fuel crud must be via post-shutdown formation, either the result of oxidizing conditions at shutdown, or storage of the fuel in air-saturated spent fuel pool water. The presence of colloidal goethite in the filter cake samples, but not in the crud flakes, suggests that the goethite collected on filter papers could have been formed upon exposure of crud to oxidizing conditions during transfer and storage in the spent fuel pool.

Several other compounds were also considered during the analysis of the Mössbauer spectra: Iron borate ($FeBO_3$), an antiferromagnet with Néel temperature of 348 K, exhibits at room temperature an internal hyperfine magnetic field of $H = 33$ T, a quadrupole splitting of $\Delta E_Q = -0.38$ mm/s, and a centroid shift of $\delta_{Fe} \sim 0.3$ mm/s, typical of Fe^{3+} [26]. In view of the similarity of these parameters to the Mössbauer parameters of goethite, the presence of a small amount of this material cannot be excluded in the filter cake samples. Iron orthoborate (Fe_3BO_6), a weak antiferromagnet with a Néel temperature of 508 K, exhibits at room temperature two sextets with hyperfine magnetic fields of $H = 42.6$ T and 45.8 T. The sextets are ascribed to two different Fe^{3+} octahedral sites, with both the site occupancy and spectral intensity ratio equaling 1:2. The values of δ_{Fe} and ΔE_Q have not been reported for this compound. A very small fraction of Fe_3BO_6, less than 1–2% Fe, is not ruled out within the spectral resolution in the Callaway crud. Another possible compound known to form in Ni-Fe-B-O systems, a Ni–Fe borate ($NiFeBO_4$), yields at room temperature a quadrupole splitting of $\Delta E_Q = 71$ mm/s and a centroid shift of $\delta_{Fe} = 0.44$ mm/s [18]; the spectral component that has these parameters has not been identified.

Tin, which is the alloying element of Zircaloy (about 1.5 wt%) and Zirlo (about 1.0 wt%), was found at a concentration (0.7 wt%) in the Callaway crud samples (see Table 5). Mössbauer emission spectra of 23.9 keV γ-rays from ^{119m}Sn in the crud samples were obtained using a polycrystalline SnO_2 absorber. As seen in Fig. 4, the spectra of the filter cake and flakes were similar and closely resembled the reference spectrum of a SnO_2 absorber. Similar Mössbauer spectra of Sn^{4+} were reported previously in filtered primary coolant samples from CANDU reactors and in the oxidation products of Zircaloy [27]. The spectral parameters of crud samples have been compared with those of several reference absorbers in Table 5. The reference set included tin oxides SnO and SnO_2, metallic tin β-Sn, Zr–1%Sn alloy, as well as Zircaloy-4, and oxidized Zircaloy-4. The analysis indicates that tin in fuel crud is present either in the form of very small particles of SnO_2 or, more likely, it substitutes for isovalent Zr^{4+} in ZrO_2 precipitates. The reduced oxidation state of tin, Sn^{2+}, would have easily been distinguished in ^{119m}Sn Mössbauer spectra, but it was

Table 5
Results of the ^{119}Sn Mössbauer spectroscopic analyses of crud sample #2 and of some reference samples at 295 K

Sample	δ (mm/s)	ΔE_Q (mm/s)	W (mm/s)
Crud samples			
#2 flakes	−0.17(1)	0.94(2)	1.48(6)
#2 cake	−0.14(1)	0.84(2)	1.57(4)
Reference data [27]			
SnO_2	−0.02(1)	0.57(1)	1.04(1)
SnO	2.67(1)	1.34(1)	1.25(1)
β-Sn	2.49(1)	0.43(1)	0.94(1)
Zirlo	1.67(1)	0.47(1)	0.74(1)
Zircaloy-4	1.71(4)	0.34(1)	0.76(2)
Zircaloy-4 oxidized 700 °C/1 d	0.05(1)	0.63(2)	0.99(5)
Sn in CANDU coolant	0.00 (1)	0.88(14)	0.58(31)

δ is the isomer shift with respect to the reference $Ca^{119m}SnO_3$source, ΔE_Q is the electric quadrupole splitting, and W is the full linewidth. Last digit(s) errors are given in parentheses.

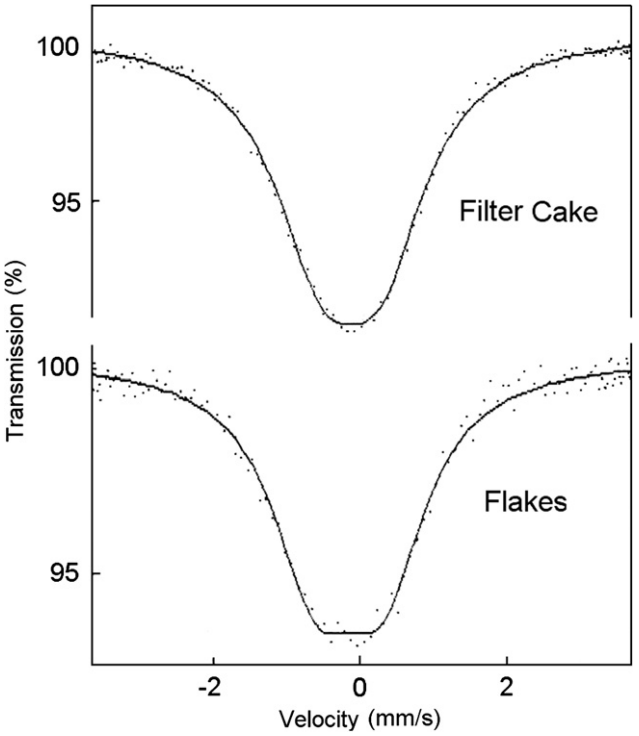

Fig. 4. ^{119m}Sn Mössbauer emission spectra of #2 fuel crud samples obtained at 295 K with a SnO_2 absorber. Top: filter cake. Bottom: loose flakes.

not observed either in filtered CANDU coolant samples or in the Callaway samples.

3.3. X-Ray diffraction analysis

X-ray powder diffraction on plate-mounted samples was carried out with a Philips Analytical diffractometer using Cu$K_{\alpha 1}$ radiation (40 kV, 120 mA) monochromatized with curved pyrolytic graphite. Scans were made in the 2Θ range from 10° to 80° in 0.02° steps and a fixed counting time per step. The flake pattern was obtained from a ~3-mm^2-sized flake from sample #1 that was crushed to make a powder sample and flat-plate mounted on a thin glass plate. The filter cake pattern was obtained for a 1-cm^2 segment of the #2 filter. Both patterns are very complex, as is seen in Fig. 5. They are compared with the diffraction patterns of reference samples of Ni_2FeBO_5, NiO, $NiFe_2O_4$ and *m*-ZrO_2, mixed in proportions 25:25:25:25 wt% and 40:10:10:40 wt%. The individual diffraction patterns of NiO, $NiFe_2O_4$, Ni_2FeBO_5 and *m*-ZrO_2 are shown in Fig. 6.

The weight fractions of the various crystalline phases in crud were determined by comparing the intensity of diffraction lines with the respective lines in reference samples. A strong and well-resolved 111 peak of *m*-ZrO_2 was used

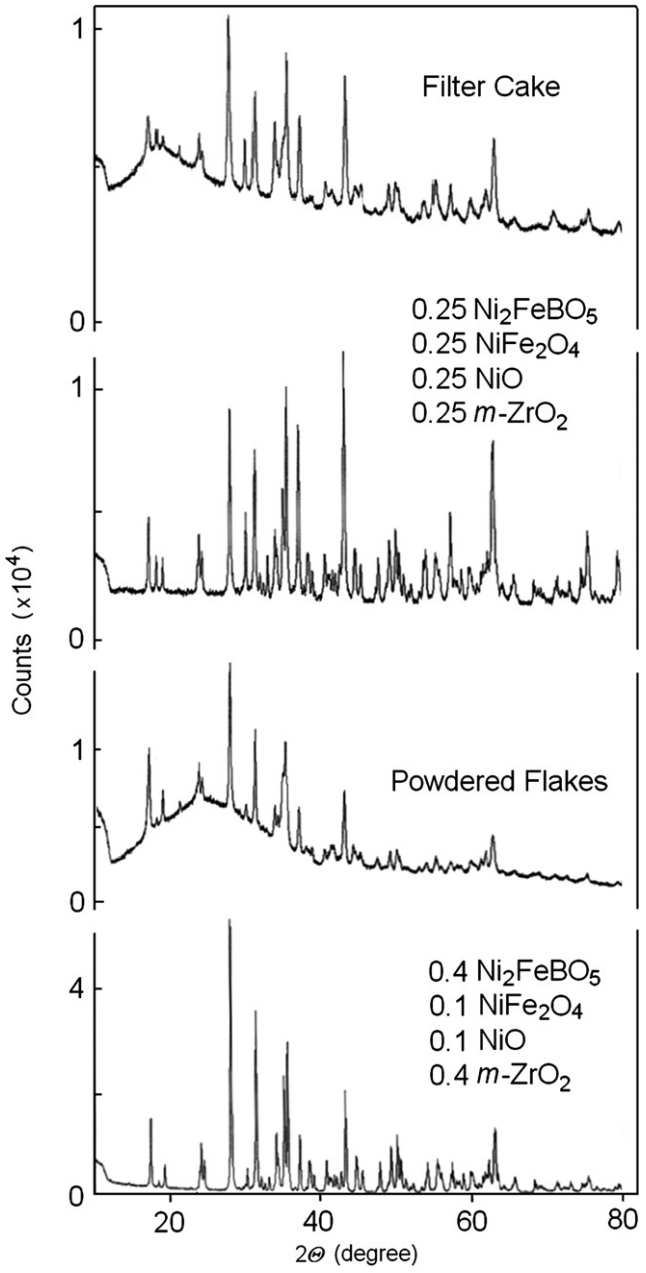

Fig. 5. X-ray powder diffraction patterns of two fuel crud samples and two synthetic reference samples.

for intensity normalization. The crud flake pattern indicated prominent diffraction peaks at 2Θ angles expected for Ni_2FeBO_5 (50 wt%), *m*-ZrO_2 (30 wt%), NiO (10 wt%), and $NiFe_2O_4$ (10 wt%). The crud cake pattern could be best described as a mixture of Ni_2FeBO_5 (40 wt%), *m*-ZrO_2 (30 wt%), NiO (15 wt%), and $NiFe_2O_4$ (15 wt%). Neither Ni metal nor inclusions of tetragonal ZrO_2 were seen in these diffraction patterns.

A comparison of the ratios between weight fractions of Ni_2FeBO_5 and $NiFe_2O_4$ determined from XRD (5.0 for #1 flake and 2.7 for #2 filter cake) and Mössbauer spectroscopy (6.1 and 4.2, respectively) shows a rather good agreement between the two methods.

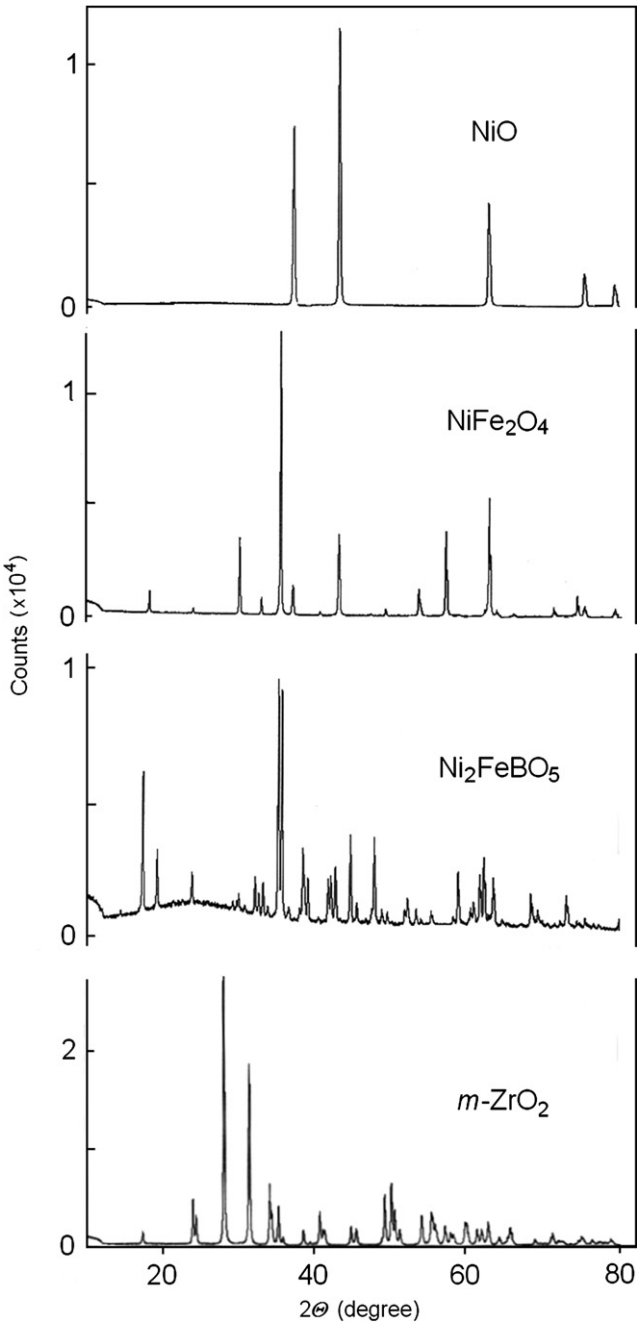

Fig. 6. X-ray powder diffraction patterns of individual reference specimens.

3.4. Elemental analysis

These analyses presented the challenge of developing procedures for dissolving reactor crud on filter paper or as loose crud flakes, with quantitative recovery of boron. The analyses were initially hampered by the inability to dissolve the entire sample; large amounts of residue remained after digestion that could not be dissolved in mixed HCl, HNO_3 and HF. As noted above, Ni_2FeBO_5 is very difficult to dissolve, eliminating the possibility of using a simple acid dissolution procedure. Conditions aggressive enough to dissolve the sample would also partially volatilize the boron. Several fusion–dissolution techniques were investigated and the efficiency of dissolution was found to be best after fusion with Na_2O_2. After the sodium peroxide fusion, the acid dissolution was complete, boron recovery was excellent and contamination was low.

Once dissolved, B, Fe, Ni, Zr, the $^{10}B/^{11}B$ isotopic ratio, and various impurities could be measured by a combination of inductively coupled plasma (ICP), atomic emission spectroscopy (AES) and mass spectrometry (MS). A Perkin Elmer Optima 3300 ICP–AES instrument and a Varian Ultramass ICP–MS instrument were both configured for radioactive work. Examples of the results are presented in Table 6. The analysis of the synthetic Ni_2FeBO_5 sample gave Ni, Fe, and B in agreement with its chemical formula. A 2-cm^2 segment of sample #1 filter and 2.6 mg of sample #1 crud flakes were then successfully fused and digested. Assuming that all the boron in the crud is present as Ni_2FeBO_5, the median values of the elemental analysis for the sample #1 filter cake in Table 6 yielded the following weight composition: Ni_2FeBO_5 – 26 wt%, ZrO_2 – 31 wt%, NiO – 22 wt%, and $NiFe_2O_4$ – 21 wt%, in fairly

Table 6
Results of ICP–AES and ICP–MS analyses for reference Ni_2FeBO_5 and filter #1 samples

Element	Ni_2FeBO_5 (μg/g)	Filter #1 (2 cm^2) (μg/sample)	Flakes #1 (μg/g)
Al	<500	<35	3400 ± 600
B	42000 ± 5000	38 ± 3	23000 ± 3000
^{10}B, %	–	11.5 ± 0.3	10.2 ± 0.2
Ca	<13000	<250	<60000
Co	180 ± 60	1.3 ± 0.6	500 ± 120
Cr	<120	64 ± 4	2800 ± 300
Cu	<200	3.5 ± 1.0	1700 ± 400
Fe	213000 ± 20000	570 ± 35	109000 ± 11000
K	<6000	<110	<4000
Li	<140	4.0 ± 1.5	1000 ± 3000
Mg	<30	1.1 ± 0.4	<10000
Mn	120 ± 40	18.5 ± 1.0	7500 ± 800
Ni	441000 ± 50000	1220 ± 75	320000 ± 30000
Si	n/a	n/a	12000 ± 6000
Sn	n/a	n/a	7000 ± 4000
Zr	n/a	840 ± 50	134000 ± 13000

n/a – not analyzed.

good agreement with the XRD results for another part of this sample. A similar calculation for the sample #1 flakes yielded the following weight composition: Ni_2FeBO_5 – 60 wt%, ZrO_2 – 18 wt%, and NiO – 22 wt%, with too little Fe remaining to account for any $NiFe_2O_4$. Some $NiFe_2O_4$ could be present in this sample if one assumes the extremes of the experimental errors for the B, Fe and Ni analyses. Based on several assays, elemental analysis by ICP–AES showed that the boron concentration increases with an increasing Ni/Fe ratio in the crud samples.

Boron isotopic measurements by ICP–MS were made on the Na_2O_2-fused and completely dissolved aliquots of #1 sample. Standard reference materials, with certified values for the boron isotopic ratio, were used to correct for mass bias in the ICP–MS. The measured ^{10}B isotopic fraction in the filter cake was $11.5 \pm 0.3\%$, whereas the flakes gave $10.2 \pm 0.2\%$. This latter value was obtained for a significant mass of the flakes (2.6 mg); thus, the reported ratio is reasonably representative of the average value for the crud under this study. Note that these values are significantly lower than the 19.9% abundance of ^{10}B in natural boron and about 17% abundance of ^{10}B measured in reactor coolant at the end of Cycle 9.

3.5. Auger electron spectroscopy

Scanning Auger electron microscopy was used to determine the presence of boron at the surface of the crud flakes and the Ni_2FeBO_5 needles. The measurements were carried out on a Perkin Elmer PHI 670 Auger Nanoprobe equipped with a Schottky field-emission electron gun for high brightness and 20-nm spatial resolution, a cylindrical-mirror electron analyzer, a NORAN EDX system for X-ray analysis, an ion gun for removal of surface layers by sputtering, and *in situ* fracture capability. The electron energy of 3 keV was chosen because it gave the best boron-to-oxygen signal ratio. Auger electrons were measured at energy ranges between 0 and 1000 eV, permitting the identification of the principal Auger electron peaks of interest: *KLL* peaks for B at 179 eV, C at 272 eV, N at 379 eV, and O at 503 eV; and *LMM* peaks for Fe at 598, 651 and 703 eV, and Ni at 848 eV (less intense peaks were measured at 783 and 716 eV). Zr has an MNN peak at 147 eV, but it is of low intensity. The penetration depth of Auger electrons, that is, the sampling depth, was about 5 nm for Fe and Ni, and less than 1 nm for B and Zr, making the detection of B and Zr very difficult.

The Auger electron spectra of a reference sample of boron nitride (BN) and a synthetic sample of Ni_2FeBO_5 are shown in Fig. 7, along with the Auger spectrum of a sample #1 crud flake sample. The freshly fractured surface of BN gave the Auger peaks of B and N near 180 eV and 380 eV, respectively, with some contamination by C and O, as shown in Fig. 5 (top). Despite the low energy (3 keV) and current (7.6 nA) of the primary electron beam, as well as the steep sample-tilt angle (30°–40°), peak shifts of about 10–20 eV were observed due to strong sample

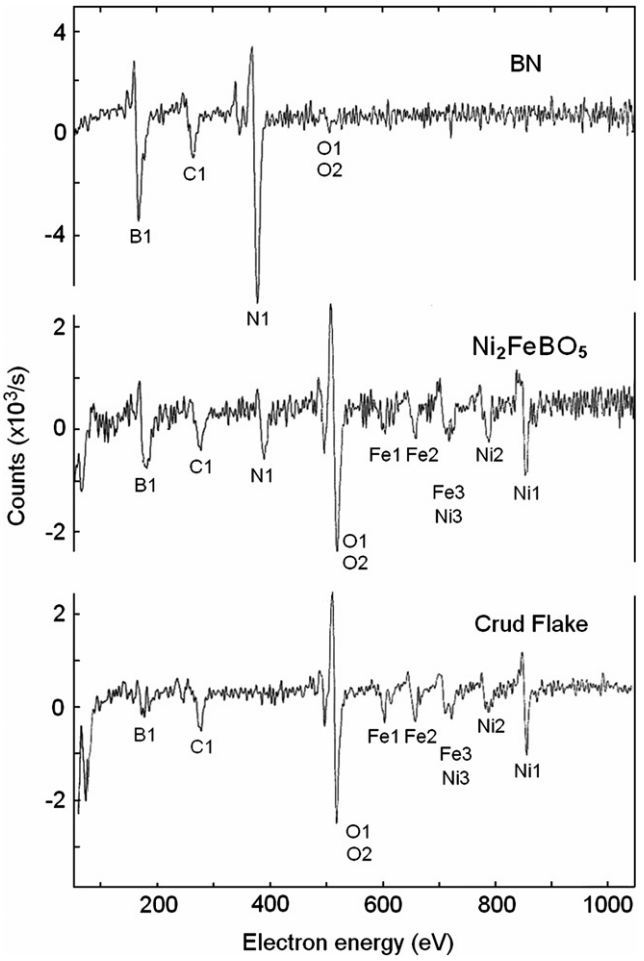

Fig. 7. Auger electron spectra of fracture surface of boron nitride reference sample (top); fracture surface of synthetic Ni_2FeBO_5 (middle); and argon-beam-sputtered surface of Ni_2FeBO_5-rich area of the crud flake (bottom).

charging effects. The Auger spectra of the fractured synthetic Ni_2FeBO_5 surface (middle) and the Ar-ion-sputtered crud flake surface (bottom) show similar peaks of Ni, Fe, O, and B. The KLL Auger lines of carbon were also observed in all samples, but these were likely from air or water contamination. The crud sample may also have had a small 260 eV LMM peak of potassium. Lithium is very difficult to observe by this method because it has only a very low-energy 45 eV KLL line within a region of secondary Ni and Fe lines.

Semi-quantitative analysis of the Auger spectra was based on published peak-to-peak amplitudes of selected lines and graphs of relative sensitivity factors $S(E_p)$ for Ni, Fe, B, O, and N at $E_p = 3$ keV. This method was subject to errors due to matrix effects on electron escape depths and backscattering factors, chemical effects on peak shapes and surface topography. This method also did not include any scale factors. The reference sample of BN yielded an approximate elemental concentration ratio of B:N = 57:43. Similarly, the reference sample of synthetic Ni_2FeBO_5 gave the proportion of elemental concentrations

as Ni:Fe:B:O = 25:10:33:36. The Ni_2FeBO_5-rich crud sample gave Ni:Fe:B:O = 32:10:17:38, in fair agreement with the chemical formula. The derived compositions are somewhat high in boron and low in oxygen – a likely result of preferential sputtering of oxygen during the removal of surface contamination by the argon ion beam.

3.6. Topography and morphology of samples

Small fragments of crud filters and numerous crud flakes were examined using scanning electron microscopy (SEM). A JEOL JXA-840A electron microprobe analyzer, adapted for handling radioactive samples of high specific activity, was used. The samples were mounted with double-sided conducting carbon tape on aluminum stubs, and were then gold-coated under vacuum. Examples of SEM micrographs of crud flakes are shown in Figs. 8–11. In general, the micrographs show crystallites of two different shapes: (1) globular particles (small spheres or polyhedrons) mostly about 1 μm in diameter; and (2) long, slender acicular particles (needles, rods, fibers, hairs), typically about 10 μm long and about 0.1 μm thick (see Fig. 9). Needles were common in some areas where they formed a felted matrix (compare plates at the bottom of Fig. 8). The stereo SEM method was used to better visualize and measure the depth of the topographic features, such as chimneys, voids, cavities, etc., in selected crud flakes. In particular, stereo images showed numerous deep pores and cavities; the 'chimneys' of fuel deposits. The stereo images also showed that the matted matrix of needles lining the channels is very porous and that the individual needles in the chimneys were markedly thinner and longer than those in the mat.

Energy-dispersive X-ray spectra (EDS) were recorded using a Norvar Si(Li) X-ray detector with a very thin sapphire window. A 25-keV electron microbeam was usually used to examine an area about 2 μm in diameter. In order to better quantify zirconium, EDS measurements were also performed with a 35-keV electron microbeam. The X-ray counts were corrected for dead time, background and instrumental drift; they were also adjusted by making matrix corrections for inter-element effects. A 'standardless' quantitative ZAF method was used to correct the intensity ratios (K ratios) of nickel, iron, zirconium, and other elements for the following effects: atomic number (Z), which takes into account the mean ionization potentials and the backscatter correction; absorption (A), which corrects for the take-off angle, i.e., the path length traversed by the X-rays, and the X-ray distribution; and fluorescence (F), which takes into account the concentration of elements present in the sample. Several characteristic points examined by EDS are depicted in Fig. 9. Examples of ZAF-corrected EDS data for characteristic crud features are listed in Table 7. It is to be noted that the complex, porous nature of the crud samples reduces the accuracy of ZAF corrections and the overall accuracy of quantitative analysis of their elemental composition. Note also that the determination of boron was not possible by the EDS technique because of the very low fluorescence yield of boron and the very small penetration depth of its X-rays.

Quantitative examination of a number of crud flakes yielded the following results. Typically, the areas densely

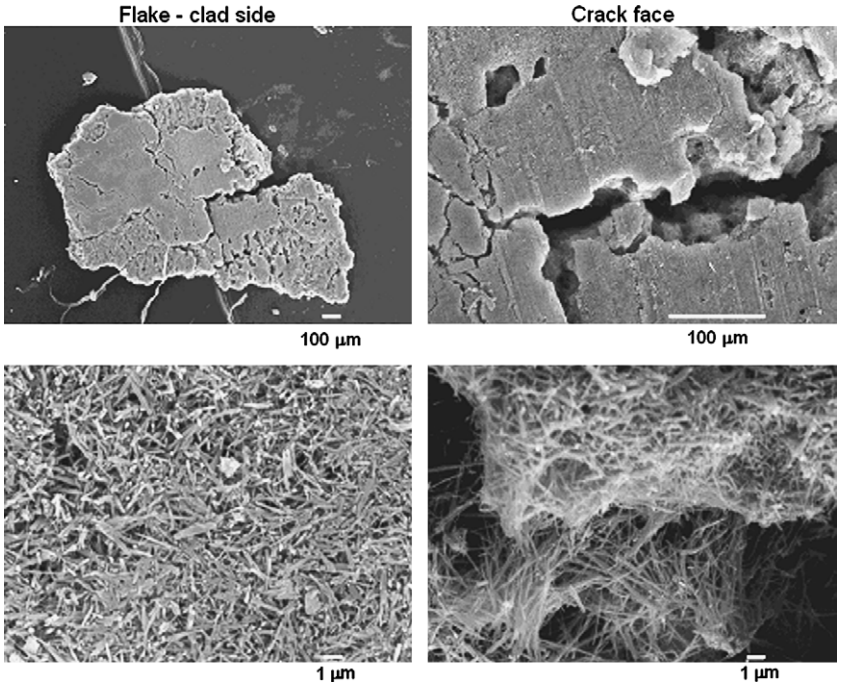

Fig. 8. SEM micrographs of a #1 crud flake taken at various magnifications. Left: flat cladding-side of flake. Right: crud near fissures or cracks.

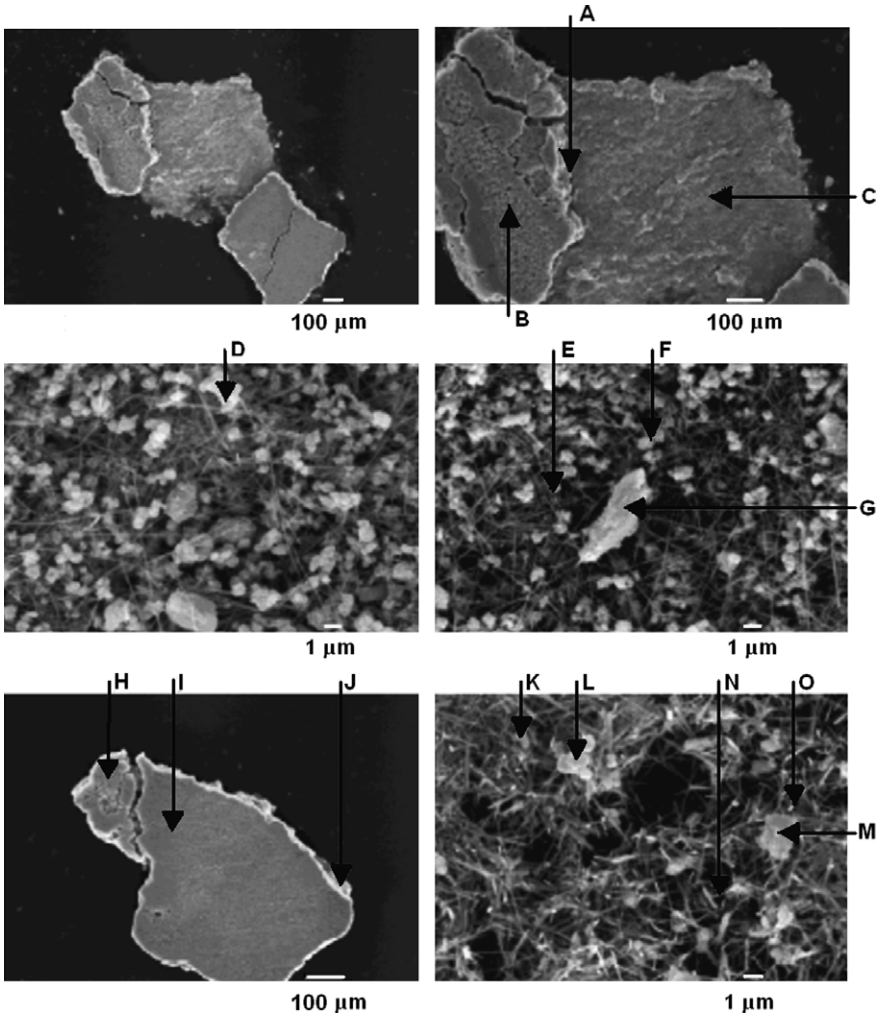

Fig. 9. SEM micrographs of two #2 crud flakes obtained at various magnifications. Pointers indicate spots analyzed by EDS, as listed in Table 7.

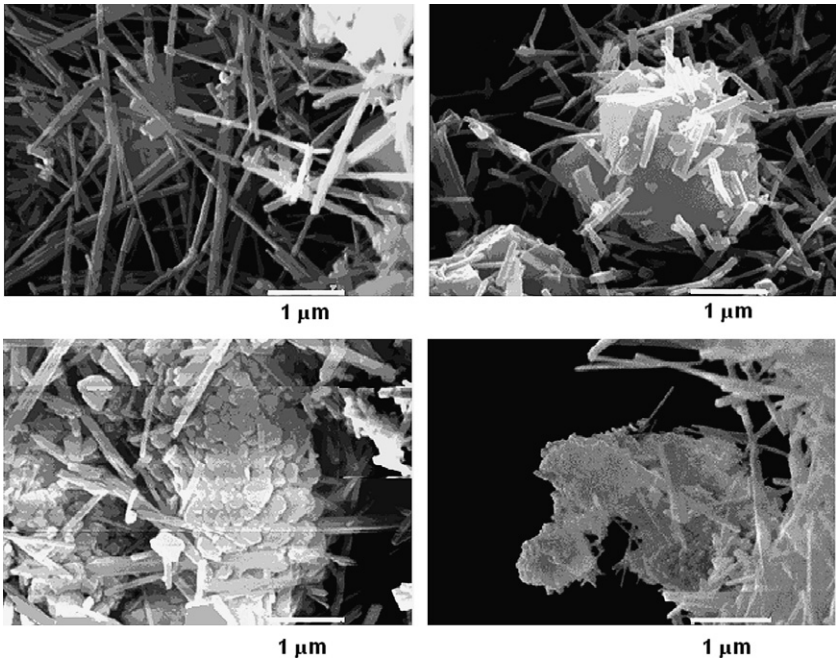

Fig. 10. SEM micrographs of a #2 crud flake, showing characteristic structural details of the different crud components.

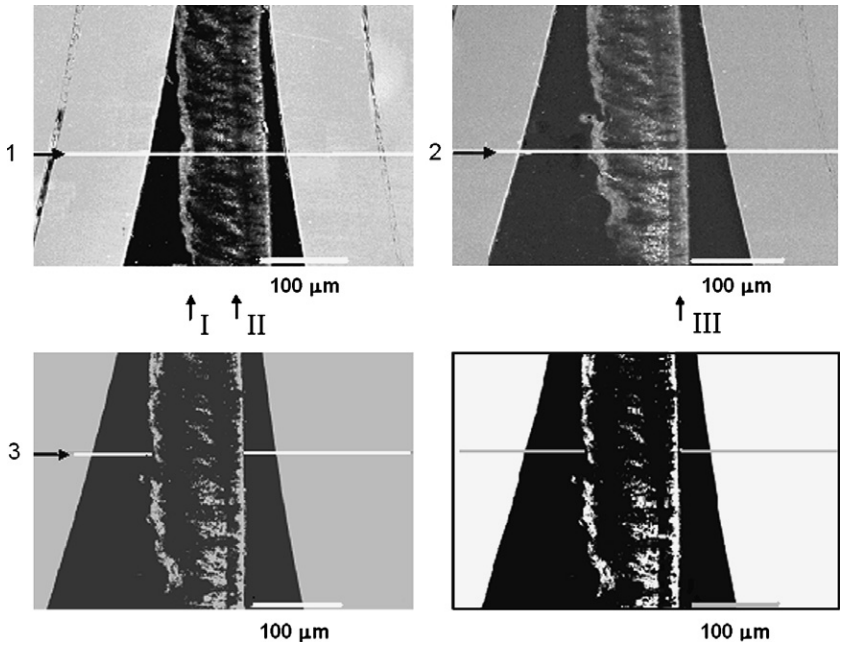

Fig. 11. Top: SEM micrographs of a mounted crud flake. A stainless 304 steel mounting clip is seen to the far left and right as grey areas. The straight side of the flake on the right is the fuel-clad side. The irregular left side of the flake is the side exposed to the coolant. Bottom right: backscattered electron (BSE) image of a polished sample of the crud flake, compared with SEM image of the same area shown on the left. Horizontal lines and pointers indicate approximately the direction in which the line profiles were taken.

Table 7
SEM–EDS data for Callaway fuel crud samples

Sample/area in Figs. 8 to 10	Sampled feature	Ni	Fe	Zr	Mn at.%	Si	Cr	Mg	Sn
#1 flakes	No electron beam	–	13.0	–	87.0	–	–	–	–
	General area	50.2	40.1	–	3.7	5.5	0.5		n/a
	Needles	44.0	26.9	2.2	n/a	n/a	n/a	n/a	n/a
	Large crystal	16.1	50.5	0.4	n/a	n/a	n/a	n/a	n/a
	ZrO_2 aggregate	10.0	5.6	81.8	n/a	n/a	n/a	n/a	n/a
	NiO aggregate	32.1	5.3	3.5	n/a	n/a	–	–	n/a
#2 flakes	General flat area	58.0	27.8	7.7	2.8	2.7	n/a	1.1	n/a
	Rough area, 200×	42.5	21.3	32.1	n/a	0.7	2.9	n/a	0.6
	Rough area, 1000×	82.3	10.1	4.4	n/a	0.5	1.3	n/a	0.7
	General flat area	63.0	31.8	n/a	1.9	3.3	n/a	n/a	n/a
	Zirconia particle	5.2	6.1	85.3	1.2	2.3	n/a	n/a	n/a
	Flake-shaped particle	51.0	26.8	13.2	2.4	6.5	n/a	–	n/a
	Needles in chimney	56.6	22.8	12.2	3.7	2.7	n/a	–	n/a
	Half-depth on edge	59.8	31.9	4.6	2.5	1.2	n/a	–	n/a
A	Flattened flake surface	57.5	27.6	7.7	2.3	4.8	n/a	–	n/a
B	Flattened area	61.9	30.0	n/a	4.2	2.2	n/a	1.7	n/a
C	General rough area	66.3	9.4	16.6	4.6	3.1	n/a	–	n/a
D	Cluster of white particles	75.2	4.1	13.7	2.1	4.9	n/a	–	n/a
E	Single white particle	61.0	10.1	18.0	3.7	4.5	2.7	–	n/a
F	Another white particle	64.2	9.8	15.3	3.0	3.6	2.5	1.6	n/a
G	Zirconia particle	13.1	3.7	75.1	4.5	3.7	n/a	–	n/a
H	General flat area	57.2	27.7	7.7	2.9	4.5	n/a	–	n/a
I	General rough area	56.3	26.9	8.8	2.9	3.4	0.9	0.7	n/a
J	On the edge	48.6	17.5	24.4	4.2	3.9	–	1.4	n/a
K	Large white particle	46.9	32.8	13.2	2.3	2.9	1.9	–	n/a
L	Single white particle	62.1	19.5	10.3	1.8	4.9	0.3	0.8	n/a
M	Cluster of white particles	26.5	26.5	38.9	2.9	4.3	1.1	–	n/a
N	Cluster of needles #1	59.1	26.4	8.0	3.1	2.8	0.5	–	n/a
O	Cluster of needles #2	59.4	26.4	7.0	2.9	3.6	0.7	–	n/a

n/a – not analyzed.
The letters A to O for the #2 flakes refer to the areas indicated in Fig. 9.

covered by needle-like particles on the clad-side of the flakes, as well as the very thin fibers reaching deep into the chimneys, consistently showed a Ni/Fe atomic ratio close to 2. Only very few fibers were seen in the fractured areas. Here, the particles were mostly oblate and showed high Ni and Zr concentrations. In these fractures, numerous zirconium-rich particles were seen as well, mostly in the form of clusters of spherical particles having a size of about 0.1–0.3 μm. Traces of Mn, Si, Cr, and Mg occurred at concentrations greater than 1 at.%, whereas the concentration of Sn was less than 1 at.%. Some particles also contained Al, K, Zn or Ca. The content of Si and Cr could not be determined for the mounted (dipped) flakes, because silica and chromia were used as polishing pastes. Note that the concentrations of Mn in Table 7 are likely overestimated, because some of the MnK_α counts originated from the electron capture decay of ^{55}Fe in the crud. The magnitude of this effect was measured without an electron beam, and is indicated by the background results in the first row of the data in Table 7. The measurements indicate that the background of the 5.9-keV MnK_α X-rays from ^{55}Fe was about 7 times stronger than the background of the 6.4-keV FeK_α X rays from ^{58}Co. The EDS data for Mn have not been corrected for this background contribution.

Higher magnification (20 000×) yielded more detailed information about the morphology of various types of particles in the crud, as illustrated in Fig. 10. In general, Ni_2FeBO_5 particles were seen to take the form of needles or rods, an average of 10 μm in length and about 0.1 μm in thickness. At the 'flattened' surface of the crud flakes (i.e. the surface that was in contact with the fuel cladding), the structure is composed mostly of packed, felted, shorter and thicker 'rods'. The needles are thinner and hair-like on the surface of boiling chimneys. All these acicular features have atomic Ni/Fe ratio near 2, as exists in Ni_2FeBO_5.

The $NiFe_2O_4$ particles range in diameter between 1 and 2 μm, and usually have the octahedral shape that is characteristic of ferrites with a spinel structure. Some cavities were seen around the particles, suggesting that the nickel ferrite particles were formed by extracting Fe and Ni from the surrounding matrix of Ni_2FeBO_5, or alternatively, that the formation or positioning of Ni_2FeBO_5 was retarded in the proximity of the $NiFe_2O_4$ particles.

The NiO particles were found mostly on the coolant side of the crud flakes. They were often nested in the Ni_2FeBO_5 matrix, and the NiO particles also appeared to frequently overgrow some of the Ni_2FeBO_5 needles as they formed. The observed NiO particles often seemed to form clusters of tiny ~0.1-μm-sized, nearly spherical particulates.

The *m*-ZrO_2 particles consisted of aggregates of many oblate crystallites sized between 0.1 and 0.3 μm. They appeared to be clustered inside a mat of short Ni_2FeBO_5 needles, especially in the middle of the flake depth. Some of the Ni_2FeBO_5 needles appeared to have penetrated through such aggregates.

3.7. EDS mapping and line profiles

Selected samples of crud flakes were embedded in acrylic mounts and highly polished, using the procedure used for metallographic microscopy. The thickness of the examined flakes was about 100 μm. The surface of the samples was plated with a thin gold film prior to the SEM examinations. Selected SEM images obtained for one of the samples used for depth profiling are shown in Fig. 11. The most characteristic feature of the images shown in Fig. 11 is a 30–40 μm-thick band of compacted Ni_2FeBO_5 needles parallel to the clad surface. The band is especially dense at the deposit-clad interface. To the left of the Ni_2FeBO_5 band, there is an irregular bright-spotted zone about 30 μm in thickness. Here, aggregates of small particles of *m*-ZrO_2 and some NiO and $NiFe_2O_4$ are embedded in a low-density mat of Ni_2FeBO_5 needles. The distinct fishbone-like pattern of somewhat curved, alternating bright and dark areas in this zone suggests variations in density. These regions have the appearance of the boiling micro-chimneys that have been ascribed to the wick boiling mechanism [28]. An average spacing between these chimney-like features is about 30 μm. Further to the left, there is a dark, especially low-density ~30-μm-thick zone, followed further to the left by a bright irregular ~10-μm-thick coolant/flake interface consisting mostly of dense aggregates of NiO particles.

Additional information about the distribution of various phases in the crud flake samples can be obtained from backscattered electron (BSE) images. The backscattered electron coefficient is strongly dependent upon the atomic number *Z*, as well as upon the microscopic porosity of the material. Since a flat, very finely polished surface has little or no topography, most of the contrast in BSE images results from variations in *Z*, i.e. from differences in chemical composition and local density. Characteristic BSE images of the same area as the SEM image in are presented in Fig. 11 (bottom, right). The BSE images were especially effective in showing the three dense regions: (1) the dense (squashed) region of Ni_2FeBO_5 needles nearest to the surface of the cladding; (2) the irregular spots representing *m*-ZrO_2-rich regions in the center of the flake; and (3) the outer-edge region containing dense aggregates of nickel oxide particles. In this particular flake, the thinner part of the flake (at the bottom of the plates) has a larger area of *m*-ZrO_2 aggregates, which appear to be denser and more separated from each other. This seems to be associated with thinning of the Ni_2FeBO_5 zone. Fig. 12 presents digital SEM image and elemental EDS X-ray maps of Ni, Zr, Fe, Si, and Mn in a small area of a mounted flake. The characteristic elemental distributions across the flake are clearly apparent in these maps. As seen, the nickel tends to concentrate at the edges of the deposit flakes, near the cladding surface and in regions exposed to the bulk coolant. Iron tends to aggregate in the area adjacent to the clad where, together with Ni, O, and B, it forms a band of matted Ni_2FeBO_5 needles. Iron also occurs sporadically

as larger, octahedral or oblate $NiFe_2O_4$ particles that appear as bright spots. Zirconium aggregates in the central region of the flake, appearing as stripes of *m*-ZrO_2 precipitate supported by a less dense matrix of Ni_2FeBO_5 needles. Silicon follows a distribution similar to zirconium, whereas the faint traces of MnK_α X-rays suggest that these are mostly ascribed to radioactive ^{55}Fe decay, and therefore correlate with distributions of Fe and Ni.

EDS line profiles were obtained to quantify the spatial distribution of the various elements and chemical compounds comprising the fuel crud. A principal goal was to obtain SEM–EDS line profiles of Fe, Ni, and Zr across the flake, comparing elemental distributions of crud areas in contact with the clad surface to those nearer the crud–water interface. The depth distribution of Ni_2FeBO_5 and *m*-ZrO_2 across the flake was of particular interest. A further goal was to determine the variation of metal oxides and morphology across the flake (clad-side to coolant-side), and around the pores (chimneys).

The line-profiling EDS scans were performed with a 1-μm electron beam in an automatic stepwise mode with 2-μm steps. Examples of the radial profiles (in a direction perpendicular to the surface of the flake) are shown in Fig. 13. Note that the coolant side of the crud flake is on the left and the clad side is on the right, and that the high iron values at the very far right side of the profile represent the stainless steel 304 micro-clip used to mount this sample. The EDS count-rate profiles were ZAF-corrected and

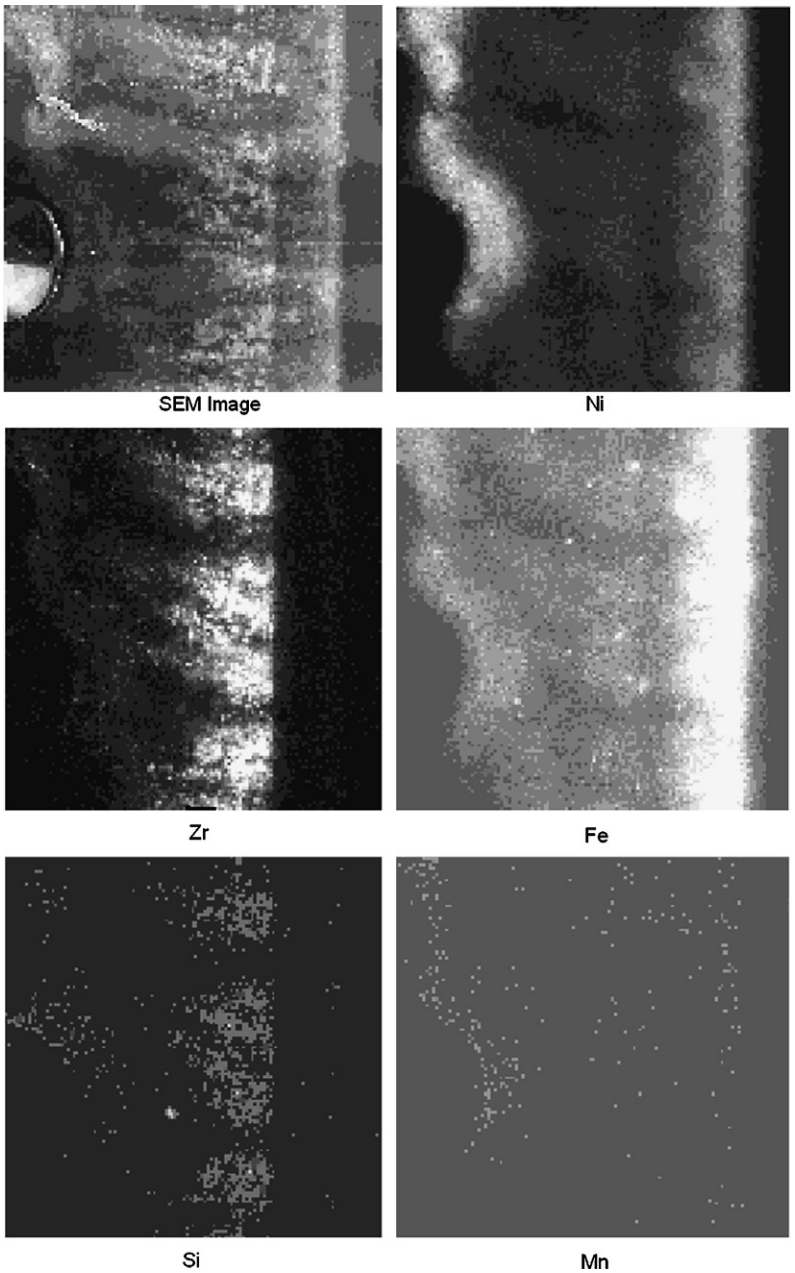

Fig. 12. Digital scanning electron microprobe elemental X-ray maps of Ni, Zr, Fe, Si and Mn in a small area of crud flake.

weight-normalized values for Ni, Fe and Zr are presented in each figure.

Note that the ZAF-corrected profiles of the various elements are not truly proportional to their concentrations in the sample. In particular, the concentration of zirconium is grossly underestimated compared to concentrations of Fe, Ni, and Cr. However, the count-rate data still provide good insight into the general features of the elements' distribution. In particular, Fig. 13 indicates that the zone with Ni/Fe ~ 2 (Ni_2FeBO_5) extends as much as 80 μm from the clad-side surface of the flake. The Ni/Fe ratio increases to 6–8 (likely the result of increasing NiO concentration) over the last 20 μm of the crud flake nearest the coolant side. In profile 2 *m*-ZrO_2 is not present in the first 30 μm from the clad side, then quickly rises to a value of about 40 wt%, followed by a gradual decrease across the remainder of the flake. The concentrations of Ni and Zr tend to vary inversely to each other. The 30–40-μm-wide Ni_2FeBO_5-rich and *m*-ZrO_2-free zone is generally parallel to the flat surface, but becomes narrower in the thinner parts of the flake.

As discussed above, neither the direct EDS count rates nor ZAF-corrected data properly reflect the relative and absolute concentrations of elements for these porous and complex samples. While better than the direct-count data, the ZAF-corrected EDS results still do not properly reflect density variations along the profiles. The flakes contain several types of particles having various shapes, sizes, and widely varying concentrations, and regions across the flake exhibit broadly varying porosity. Deriving the absolute density profiles from

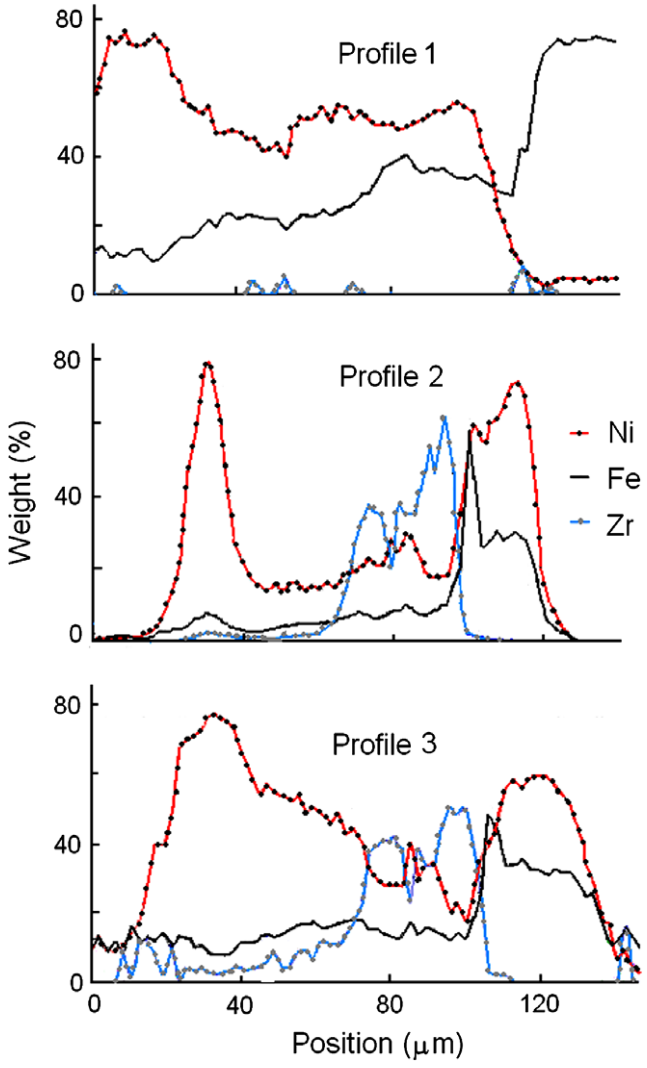

Fig. 13. EDS line profiles of Ni, Fe and Zr in mounted crud flake measured in a direction perpendicular to the flat surface of the flake and represented as ZAF-corrected data in weight units normalized to unity. The profiles were taken along lines 1 (top graph), 2 (middle graph) and 3 (bottom graph) depicted in Fig. 11. The right end of profile 1 extends to the stainless 304 steel mounting clip.

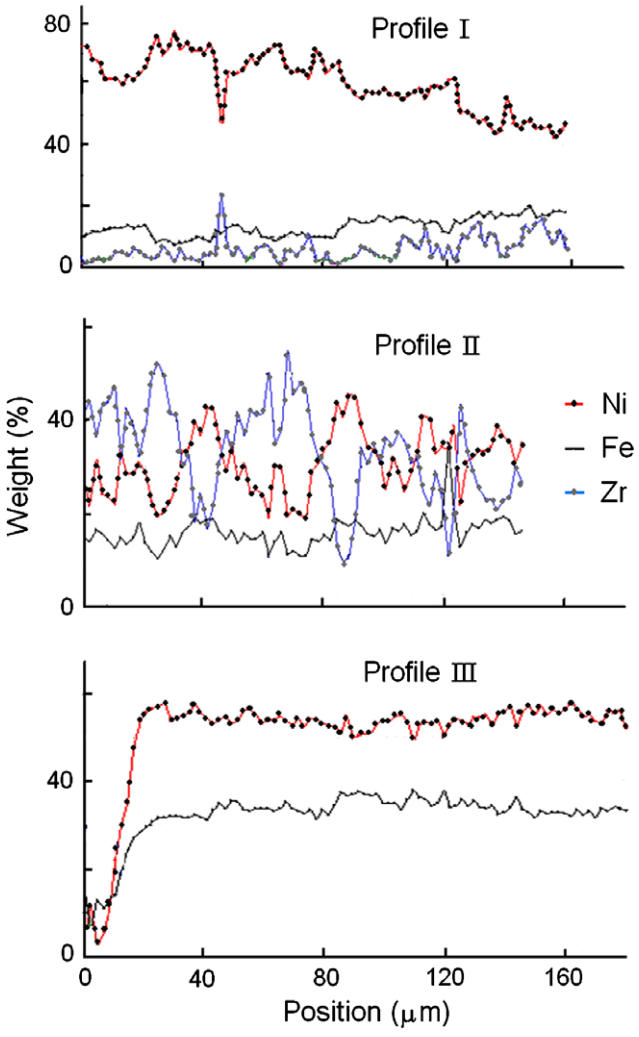

Fig. 14. EDS line profiles of N, Fe and Zr in mounted crud flake measured in a direction parallel to the flat surface of the flake and represented as ZAF-corrected data in weight units normalized to unity. The profiles were taken across the nickel oxide-rich region at the coolant side of the flake (top), across zirconium-rich central region of flake (middle), and across bonaccordite-rich region adjacent to the cladding (bottom); that is, respectively, along lines I, II and III in Fig. 11.

ZAF-corrected data for these porous and highly structured materials would demand the use of reference samples having morphologies and densities that are close to those of the actual specimens. In the absence of suitable reference samples, the EDS count-rate profile shown in Fig. 13 was calibrated by normalizing to the density of Ni, Fe, and Cr in the stainless steel 304 micro-clip that was mounted and analyzed together with the crud flake. The bulk concentrations of Fe, Cr, and Ni in SS-304 are 70.2, 20.5, and 9.3 at.%, respectively, whereas the ZAF-corrected EDS data of the micro-clip shown in Fig. 11 (bottom) gave 77, 18, and 5 wt%, respectively.

Fig. 14 compares three axial profiles, taken in three different directions parallel to the surface of the flake. As seen in the figure, the profile taken along the outer coolant-side part of the flake mostly indicates Ni consistent with a NiO-rich distribution, whereas the profile taken along the Ni_2FeBO_5-rich zone near the fuel cladding shows smooth Ni and Fe signals in a proportion close to 2. In contrast to these observations, the axial profile taken across the central zone of the flake indicates the prominent counter-oscillating character of Zr and Ni signals that reflects the aggregation of zirconium oxide particles between boiling chimneys, and possibly some excess of nickel (NiO plating) over the bonaccordite composition in the chimneys.

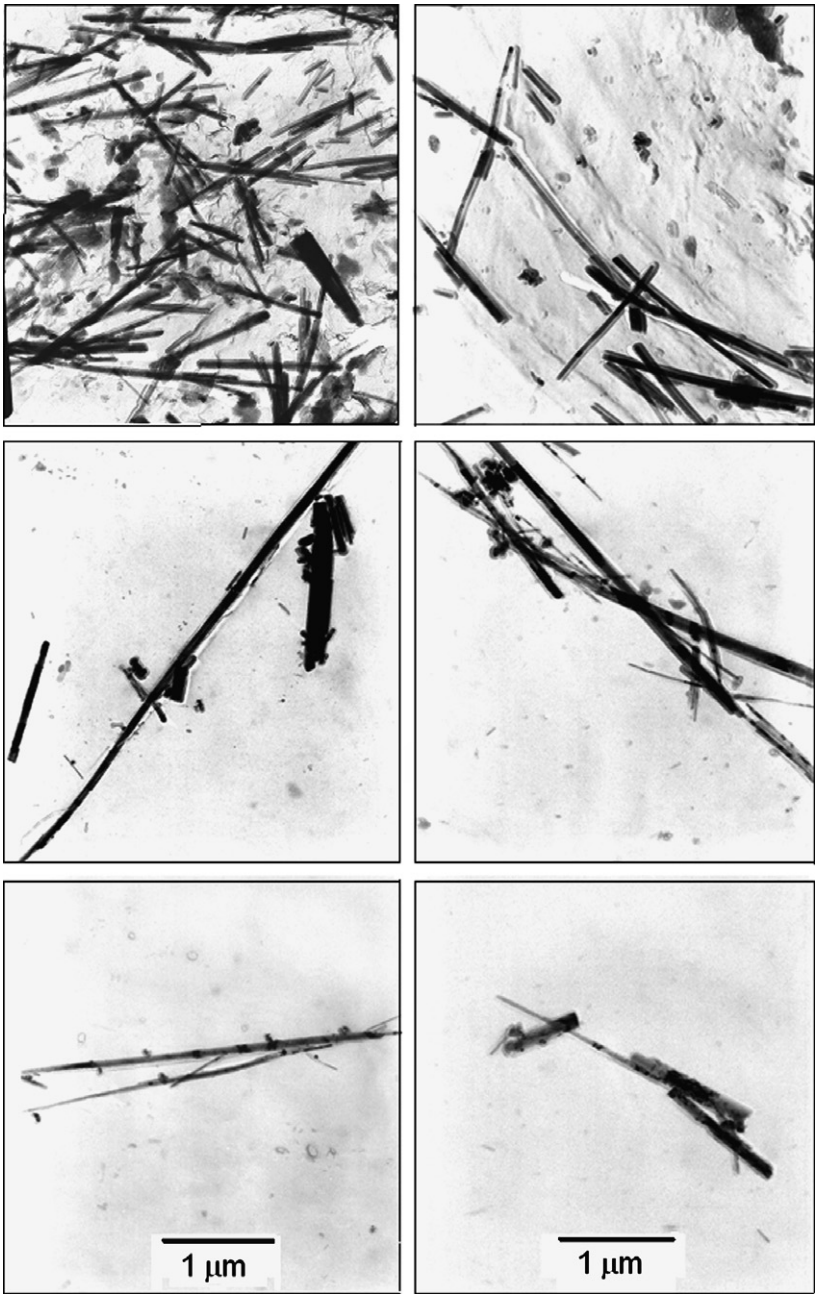

Fig. 15. Transmission electron micrographs of needle-like particles recorded in a 300 kV transmission electron microscope.

3.8. Transmission electron microscopy

Electron-transparent specimens suitable for transmission electron microscopy (TEM) study were prepared using an extraction replica technique. The extracted needle-shaped particles were supported on a thin carbon film on a 100-μm-sized copper grid. The needles, being $\leqslant 0.1$ μm thick, were transparent to the 300 keV electron beam. Fig. 15 presents examples of transmission electron micrographs showing the distribution of needles extracted from the crud samples.

X-ray spectra acquired from the needles showed the presence of Ni, Fe and O. The intensity ratio of the NiK_α to FeK_α X-ray peaks was about 2, in accord with the formula of Ni_2FeBO_5. A weak line was observed at about 0.2 keV that may be interpreted as the BK_α line. Detection of minor quantities of boron in samples of Ni_2FeBO_5 is difficult because the BK_α X-rays are of low intensity compared to other X-rays produced in the sample. For a thin (<10 nm) TEM specimen containing two or more elements, the intensity ratio of K_α X-rays for those elements is given by the proportions $I_1/I_2/\ldots = c_1Z_1/c_2Z_2/\ldots$, where c_1, c_2 ... are the concentrations, and Z_1, Z_2 ... are the atomic number corrections for elements 1, 2, etc. According to this approximation, the estimated intensity ratio of the K_α X-rays emitted from Ni_2FeBO_5 should be roughly Ni:Fe:O:B = 10:5:8:1. This is in fair agreement with the observed intensity ratio of the K_α lines in TEM–EDS spectra.

The X-ray maps of needles obtained in the scanning TEM mode are shown in Fig. 16. The maps clearly illustrate that Ni, Fe, and O are similarly distributed in the needles, consistent with the chemical formula Ni_2FeBO_5. As explained above, the X-ray map did not show any boron because of the very small signal-to-noise ratio in the region of the BK_α line. This inherently poor detection of boron X-rays could explain why this element has not been identified in PWR fuel crud before now. However, it was demonstrated above that boron *can* be detected directly in fuel crud samples by means of scanning Auger microscopy (SAM), because the Auger electron yields for light elements such as boron are generally much higher (close to 1) than the X-ray fluorescence yields. Convergent electron beam diffraction (CEBD) patterns were examined using a convergent electron beam 10–100 nm in diameter. The diffraction patterns from various zones of the needles were analyzed using stereographic projections, and were indexed consistent with the orthorhombic crystal structure and the unit cell parameters of Ni_2FeBO_5, i.e. $a = 0.9213$ nm, $b = 1.2229$ nm, and $c = 0.3001$ nm [16]. In addition, the c-axis was found to be parallel to the long axis of the needle, in agreement with the findings for ludwigite [14,15].

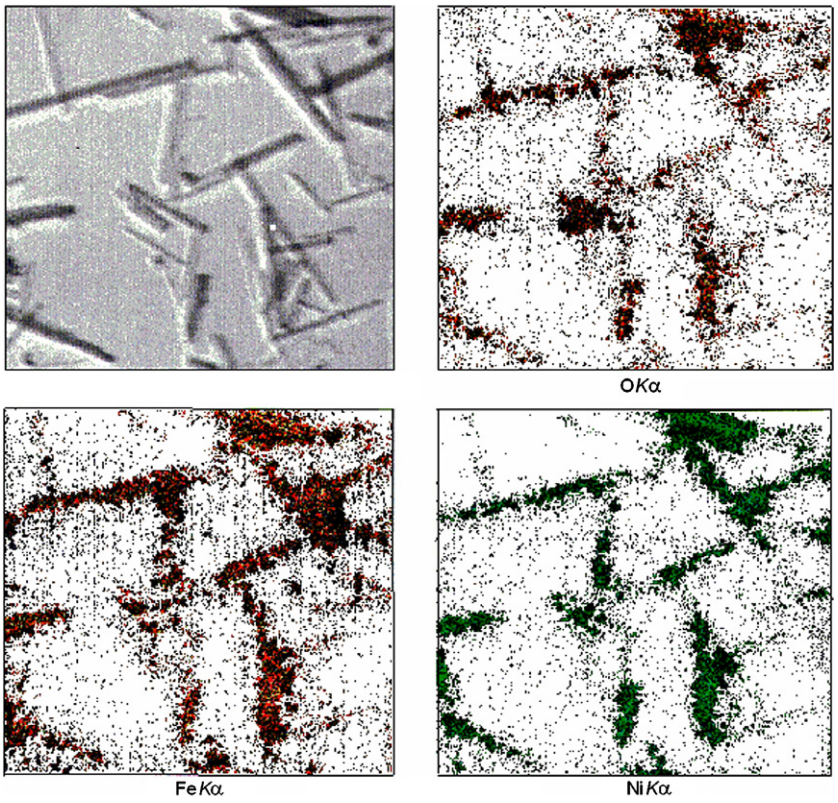

Fig. 16. Scanning TEM image of a small fragment of a sample and correlated elemental maps of oxygen, iron and nickel obtained by recording respective K_α X-rays.

4. Discussion of results

The analyses of Callaway Cycle 9 fuel crud samples reported in this work were intended primarily to determine the chemical form and the oxidation state of iron-bearing oxides. The crud flakes were found to contain predominantly nickel-iron oxyborate (Ni_2FeBO_5, bonaccordite), roughly in the amount of 50 wt%, and monoclinic zirconium oxide (m-ZrO_2, badelleyite), in the amount of about 30 wt%. The nickel ferrite ($NiFe_2O_4$, trevorite) and nickel oxide (NiO) commonly observed earlier in PWR crud samples represented only small fractions (about 10 wt%) of the deposits. Thus, these results present the first definitive observation of Ni_2FeBO_5 and m-ZrO_2 particles in PWR fuel deposit samples; such novel types of fuel deposit components have not been reported in the past.

Fuel crud deposits in PWRs have been commonly known to consist largely of tenacious deposits of $NiFe_2O_4$, normally of more or less stoichiometric composition [29]. In particular, in an early SEM study of Ni-rich (Ni/Fe ratio about 5) crud flakes from Callaway Cycle 9 spanning five fuel rods, the deposits were identified as a mixture of $NiFe_2O_4$ and NiO microcrystals [11]. This behavior is illustrated by Westinghouse data compiled between 1973 and 1996 for 238 crud samples from low power to moderate- and high-power PWR fuel rods in plants having Alloy 600 steam generators [11]. According to these data, the Ni/Fe distribution frequency showed a Gaussian-shaped peak at Ni/Fe $\sim$ 0.5. Only in 26 cases was the Ni/Fe ratio between 1 and 6; sixteen of these cases were for low-power fuel rods and 10 for moderate- to high-power fuel rods. Such sporadic occurrences of high Ni/Fe ratio were ascribed to high NiO content in some of the samples.

Nickel oxide can be formed under an excess concentration of Ni at somewhat higher temperatures than iron oxide, and in an oxidizing atmosphere. There have been only a few cases of NiO being detected in crud. The large amount of NiO detected in the present study suggests that the concentration of Ni in Callaway reactor water is considerably higher than one-half that of Fe, and higher than the at-power solubility of NiO (about 0.2 ppb). Analyses of primary coolant grab samples for 11 PWRs showed Callaway to have in 1990–2000 period a very high nickel concentrations (11 ppb at BOC and 53 ppb at EOC), while plants without AOA typically had Ni concentrations in the range of 1–5 ppb [30]. Also, Callaway's average EOC values for ^{58}Co in coolant samples were more than twice those of other plants. The iron concentration in Callaway's coolant is also high (12 ppb at EOC and 17 ppb at BOC), but no correlation was established between Fe concentrations and the magnitude of AOA.

The Ni/Fe concentration ratio in fuel crud may be an indicator of the conditions under which the PWR reactor has operated. A ratio of Ni/Fe near 0.5, reflected by a low EOC $^{58}Co/^{60}Co$ activity ratio, has long been considered an indicator of predominantly nickel ferrite in PWR fuel crud and of successful nickel ferrite control chemistry. However, advances in robust fuel design and attainment of high burn-up have increased shutdown nickel releases markedly at many plants. Also, the fuel crud particles in deposits from AOA plants occasionally show much higher Ni/Fe and EOC $^{58}Co/^{60}Co$ ratios, suggesting increased content of NiO or Ni metal in the crud. A high Ni/Fe ratio was also related to high levels of ^{58}Co and ^{60}Co in the reactor water, both in PWRs and boiling water reactors (BWRs), because at Ni/Fe > 2, the nickel surplus is believed to deposit on fuel rods as nickel oxide, NiO. The presence of nickel oxide in the fuel crud raises ^{58}Co and ^{60}Co in the reactor water, because NiO is more soluble than $NiFe_2O_4$.

Our first evidence for Ni_2FeBO_5 came from Mössbauer transmission spectroscopy of the 14.4 keV γ-rays of ^{57}Fe. The Mössbauer technique determined that almost all iron in the crud was in the ferric state, Fe^{3+}, partly in the form of Ni_2FeBO_5, and partly $Ni(Fe,Cr)_2O_4$ at Cr/Fe $\sim$ 0.1. The weight percentage of iron in the form of Ni_2FeBO_5 ranged from 25% in the filter cake to as high as 75% in the crud flakes. The corresponding molar ratio of iron as Ni_2FeBO_5 and as $NiFe_2O_4$ in the crud flakes was about 7. X-ray diffraction showed a complex superposition of Ni_2FeBO_5, m-ZrO_2, $NiFe_2O_4$ and NiO patterns. Synthetic samples of the various fuel crud components were prepared and scanned to quantify the XRD patterns of crud samples. The proportions of the various phases were different for the cake and flake samples. The sample #1 crud flake indicated about 50 wt%Ni_2FeBO_5, 30 wt% m-ZrO_2, and 10-wt% amounts of $NiFe_2O_4$ and NiO; the XRD of sample #2 filter cake indicated about 40 wt % Ni_2FeBO_5 and 30 wt % m-ZrO_2, in addition to 15-wt% amounts of $NiFe_2O_4$ and NiO.

High-resolution SEM images showed that acicular particles (needle-sized, about 10 μm by 0.1 μm) were densely packed at the crud-clad interface, whereas fewer, slender needles appeared at the flake-coolant interface. SEM–EDS indicated a Ni/Fe atomic ratio of about 2 in all areas containing the needles, consistent with the formula for Ni_2FeBO_5. SEM–EDS line-profiling analyses of mounted, highly polished sections of selected flakes further quantified these distributions and related them to the proposed formation and deposition mechanisms. The depth profiles revealed a 30- to 40-μm-wide zone of dense, zirconium-free Ni_2FeBO_5 on the cladding side of the flakes. NiO particles tended to be on the crud/coolant face of the flake, whereas aggregates of $\sim$1-μm-sized m-ZrO_2 particles precipitated in the central region of the flake. The average atomic ratios of Ni, Fe and B on the clad side of the flake and on the coolant side of were close to the corresponding ratios in Ni_2FeBO_5 and NiO, respectively.

The quantification of ^{10}B was performed to estimate the role of boron in neutron flux depression. Quantitative ICP–MS analysis determined the isotopic percentage of ^{10}B in the #1 fuel crud cake and flakes to be $11.5 \pm 0.3\%$ and $10.2 \pm 0.2\%$, respectively. These values are much lower than the natural abundance of this isotope (19.9%) and the abundance of ^{10}B in Callaway EOC coolant (about

17%), indicating that ^{10}B in the Ni_2FeBO_5 needles has been significantly depleted during the fuel cycle. A corresponding amount of ^{7}Li had to be formed and released into the crud matrix. Such a low percentage of ^{10}B in the crud means that the boron in it was exposed to the thermal neutron flux for at least 40 effective full-power days (EFPDs).

5. Summary and remarks

To summarize, all our results lead to the conclusion that the needle-like particles in fuel crud deposits examined in this work are composed of Ni_2FeBO_5. Bonaccordite, along with other members of the ludwigite family, is known to form particles of acicular morphology (needles, fibers, and rod-like structures). Minerals of the ludwigite type are known to form readily under hydrothermal conditions, at temperatures of about 500–600 °C. It has been shown in separate paper [7] that Ni_2FeBO_5 can be produced hydrothermally even at temperatures of 385–400 °C, and thus not much higher than the range of temperatures at the surface of fuel rods.

Accurate EDS line-profiling was found to be very useful for understanding the mechanism of crud deposition and its relationship to AOA effects. The features of Callaway Cycle 9 crud morphology observed to date have suggested specific chemical and thermal-hydraulic conditions that favour crud deposition and re-formation during the fuel cycle. In particular, the profiles suggest that the zone of dense Ni_2FeBO_5 near the surface of the fuel cladding could have been formed by hydrothermal reactions of NiO and $NiFe_2O_4$ in the presence of H_3BO_3 and LiOH accumulating in NiO–$NiFe_2O_4$ crud during the fuel cycle.

Zirconium oxide particles were found in the Callaway Cycle 9 fuel crud samples in weight fractions as high as 30%, and were entirely in the form of monoclinic zirconia, *m*-ZrO_2. The question then arises regarding the source of so much zirconia in the samples, and whether it indicates any degradation of the fuel cladding. The small size and globular structure of the *m*-ZrO_2 particles, the appearance of their aggregates, as well as their depth distribution in crud flakes, suggest that this material was re-precipitated from hydrothermal solution, and not simply scraped mechanically from the fuel surface. Such hydrothermal precipitates of ZrO_2 have been described in the literature on ceramics [31,32]. It has also been postulated that the hydrothermal re-precipitation may occur at the surface of PWR fuel at elevated pH [33,34].

The unexpectedly high fraction of *m*-ZrO_2 found in the crud is suggested to originate from dissolution of the adjacent Zirlo cladding. This may be caused during boiling in the presence of high concentrations of LiOH produced by local boiling and ^{10}B-n reactions, as suggested in Ref. [7]. A high surface pH may result in a higher chemical attack of the cladding than is usually assumed. One can further postulate that subsequent hydrothermal precipitation of colloidal *m*-ZrO_2 occurs at some distance from the fuel cladding surface because of the pH and temperature gradients established through the crud layer. A review of the studies of precipitation of zirconia particles at hydrothermal conditions strongly supports this hypothesis. Besides its importance as a measure of fuel clad corrosion, the presence of copious amounts of *m*-ZrO_2 in fuel crud may impact AOA, if it is found that this material is an efficient substrate for adsorbing boric acid from the PWR coolant.

Furthermore, our EDS depth profiles consistently showed that much of the *m*-ZrO_2 was embedded inside the crud flakes rather than attached to their surface. Such a region in the centre of the crud layer likely results from the re-precipitation of dissolved zirconium oxide along temperature and alkalinity gradients formed across the crud thickness. Thus, it is very likely that the aggregates of small *m*-ZrO_2 particles found in the middle of the crud layer are the result of dissolution of zirconium oxide on the surface of Zirlo fuel cladding and the subsequent re-precipitation from the alkaline medium at high temperatures that exist in deposits formed on high-duty fuel rods under AOA conditions. Presumably, at a distance of 30–50 μm from the clad–crud interface (where the bulk of the *m*-ZrO_2 is found), conditions of pH and temperature are such that zirconia precipitation is facilitated. Solubility data of ZrO_2 for T_{clad} will be needed to confirm this hypothesis.

It can be expected that aqueous solutions entrained by the crud layer may contain large quantities of un-dissociated H_3BO_3 and dissociated LiOH. As it was suggested elsewhere by this author [7], neutron capture reactions $^{10}B(n,\alpha)^{7}Li$ in fuel crud layers may have a significant role in affecting local microchemistry, through raising of the local temperature, alkalinity, and concentration of oxidizing radiolytic species. These effects may create chemistry conditions that exacerbate cladding corrosion and formation of Ni_2FeBO_5. The modeling of these effects is in progress.

Finding Ni_2FeBO_5 in PWR reactor crud was unexpected. This compound may have a significant and consequential bearing on understanding the near-clad chemistry of the fuel, and it may have an important role in addressing PWR water chemistry and the AOA issue. The presence of significant quantities of Ni_2FeBO_5 in the deposits constitutes another vehicle for boron retention in fuel crud, in addition to the lithium metaborate (γ-$LiBO_2$) hideout and boron chemisorption that are currently postulated to be a root cause of AOA. The relevance of this compound to AOA in high-duty reactor cores, compared to alternative means of 'fixing' boron on the fuel cladding such as lithium metaborate precipitation and boric acid physi-sorption, remains to be determined. The abundant layers of Ni_2FeBO_5 observed in thick crud flakes, which have especially low porosity near the crud-cladding interface, may play a significant role in the onset of AOA, both in the concentration of soluble species and in the retention of boron on the fuel. The measurements presented in this report showed also that the isotopic abundance of ^{10}B in the crud is considerably smaller than in natural boron

(~10% vs. 20%, respectively). Therefore, the depletion of ^{10}B and build-up of ^{7}Li through the $^{10}B(n,\alpha)^{7}Li$ reactions must be accounted for in any model of crud microchemistry in AOA-affected cores. However, this process also means that the boron in Ni_2FeBO_5 would have less impact on AOA later in the cycle, as neutrons deplete the ^{10}B.

Preparation of Ni_2FeBO_5 in the laboratory by thermal sintering and a hydrothermal method was successful, and some good reference samples were obtained by both methods. Further work should focus on finding processes for the hydrothermal formation for Ni_2FeBO_5 under PWR primary coolant conditions. The effects of Ni, Fe, B and Li concentrations, as well as pH and temperature, on Ni_2FeBO_5 formation should be further investigated. For example, one needs to determine if Ni_2FeBO_5 is stable under conditions that exist at the cladding surface early in the fuel cycle. Alternatively, does Ni_2FeBO_5 only form by rearrangement of previously deposited $NiFe_2O_4$ in the presence of boric acid and lithium hydroxide? Is boiling necessary for the formation of Ni_2FeBO_5? An understanding of these processes is crucial for developing methods of AOA mitigation and further refinement of the PWR chemistry guidelines.

6. Conclusions

Fuel deposit scrapes from span 6 of Callaway's high-AOA Cycle 9 were examined by means of a number of physical and chemical techniques. The work has provided new information about the solid-state characteristics of these deposits, their morphology and topography, phase composition and crystallographic nature, the oxidation state of metallic species, radioisotope content, and the degree of ^{10}B depletion.

The deposits were shown to be composed of ~100-μm-thick flakes having a complex internal structure. The flakes contained a large amount (about 50 wt%) of needle-like particles of the insoluble Ni–Fe oxyborate Ni_2FeBO_5, known as the mineral bonaccordite. The bonaccordite mat was notably denser in the 30–40 μm-thick layers near the clad/crud interface than in the rest of the flake. Monoclinic zirconium oxide *m*-ZrO_2 was the second largest component. Nickel oxide, NiO and nickel ferrite, $NiFe_2O_4$, comprised only a minor constituent of the crud. Nickel oxide concentrated primarily near the crud/coolant interface.

The results of this study suggest a potential direction for the next phases of the work needed to further the understanding and resolution of the AOA issue. In particular, formation of Ni_2FeBO_5 has been identified as a new mechanism for boron retention on PWR fuel. Ni_2FeBO_5 may contribute to AOA by retaining considerable amounts of boron in the fuel crud deposits. Mass spectroscopy showed that the ^{10}B abundance in the bulk of the crud is depleted from 20% to about 10–11%. It has been postulated that the neutron capture reactions $^{10}B(n,\alpha)^{7}Li$ in crud layers may play a significant role in affecting near-clad microchemistry, through raising the local temperature, alkalinity, and concentration of oxidizing radiolytic species. This information may now be used to develop a better model for crud deposition and boron retention, and to propose possible mitigation techniques for AOA.

As a result of its different chemistry, the Callaway crud was much more difficult to dissolve than conventional ferrite-based deposits. The chemistry of PWR shutdown may therefore have to be re-examined for AOA-prone plants. Reductive decomposition conditions of shutdown chemistry have been optimized for Ni-ferrite removal. Such a strategy may not be effective for removing the Ni_2FeBO_5 and NiO rich deposits from AOA cores, since Ni_2FeBO_5 remains highly insoluble under these chemistry conditions.

The methodology of fuel crud sampling must be further developed. The sampling method can be modified to collect smaller amounts of scraped material, and the crud should be retrieved quantitatively, without any contamination by fuel pool water or other extraneous material. Also, particulate sampling for PWR reactor coolant should be introduced widely as a routine tool for crud and activity transport monitoring. Characteristics of crud from such sampling should be compared with characteristics of the fuel crud scrapes.

The phase diagram of the Ni–Fe–B–Li–H_2O system must be established for hydrothermal conditions, with a focus on determining the conditions that are needed to stabilize Ni_2FeBO_5. Elevation of the pH level, resulting both from concentration due to under-deposit boiling and nuclear production of ^{7}Li in crud pores, most likely plays a significant role in the formation of Ni_2FeBO_5. Further studies of crud samples and synthetic compounds may also give insight into the electrochemical potential, effective pH, effects of radiolysis and boiling, and hydrothermal conditions at the fuel surface during crud deposition. However, projecting the laboratory results to the reactor environment will require an evaluation of the effect of radiation fields (gamma and neutron) on the chemistry of Ni_2FeBO_5 formation.

Zirconium oxide occurs as clusters of rounded, 100- to 300-nm particles of *m*-ZrO_2; it is found mostly between wick-boiling chimneys at about 20–50% of the crud depth from the clad surface. The morphology of ZrO_2 particles in fuel crud, as well as their size, depth distribution, and proportion between monoclinic and tetragonal phases, can be useful markers of hydrothermal and chemical conditions that favor the formation of these phases. Much remains to be learned in this regard through studies of transformations of ZrO_2 in pressurized high-temperature aqueous solutions. The results will be useful in developing models for corrosion product and boron deposition on high-duty fuel, as well as suggesting alternate shutdown chemistries that may be more effective for removing the highly insoluble fuel deposits in high-duty PWRs.

Acknowledgements

The research described in this paper was funded by Electric Power Research Institute' Robust Fuel Program contract WO6151-20 and is fully documented in EPRI

Report 2001, 1003129. The author would like to thank J. Deshon, Dr P. Frattini and Dr J. Blok (EPRI), G. Gary, T. Moser and J. McInvale (AmerenUE), Dr W.A. Byers (Westinghouse Electric Corporation) and Dr G. Sabol for the data on Callaway fuel characteristics, and for many helpful discussions. The valuable technical contributions of numerous AECL colleagues, especially D. Everall, M. Godin, Dr B.D. Sawicka, F. Szostak, Dr M. Totland and Dr On-Ting Woo are also greatly appreciated.

References

[1] P.L. Frattini, J. Blok, S. Chauffriat, J. Sawicki, J. Riddle, Nucl. Energy 40 (2001) 123.
[2] P.L. Frattini, T. Moser, Nucl. Energy Int. (2000). August.
[3] G.P. Sabol, J.R. Secker, J. Kormuth, H. Kunishi, D.L. Nuhfer, EPRI Report, TR-108320 ,1997.
[4] G.P. Sabol, J.R. Secker, H. Kunishi, B. Cheng, in: Proceedings of the Fontevraud IV – SFEN/ENS International Symposium on Contribution of Materials Investigation to Resolution of Problems in Pressurized Water Reactors, vol.2, September1998 p. 1159.
[5] J.A. Sawicki, in: Proceedings of the Axial Offset Anomaly (AOA) Science Workshop, Palo Alto, February 10–11, EPRI Report, Palo Alto, 1000137, 2000.
[6] J.A. Sawicki, Characterization of Corrosion Products on the Callaway Cycle 9 PWR Core, EPRI Report, Palo Alto, CA:1003129, 2001.
[7] J.A. Sawicki, in: Proceedings of Conference on Water Chemistry in Nuclear Reactor Systems, Avignon, April 22–26, 2002.
[8] J. Henshaw, J.C. McGurk, H.E. Sims, A. Tuson, S. Dickinson, J. Deshon, J. Nucl. Mater. 353 (2006) 1.
[9] B. Beverskog, Proceedings of the International Conference on Water Chemistry of Nuclear Reactor Systems, Jeju Island, October 23–26, 2006.
[10] Y. Solomon, J. Roesmer, Nucl. Tech. 29 (1976) 166.
[11] W.A. Byers, J.M. Partezana, in: Proceedings of the 1998 EPRI FWR Plant Chemistry Meeting, Huntington Beach, September 1–3, 1998, EPRI, Palo, Alto.
[12] F. Bertaut, L. Bochirol, P. Blum, Compt. Rend. 230 (1950) 764.
[13] F. Bertaut, Acta Cryst. 3 (1950) 473.
[14] Y. Takéuchi, T. Watanabé, T. Ito, Acta Cryst. 3 (1950) 98.
[15] Y. Takéuchi, T. Kogure, Zeits. Kristallogr. 200 (1992) 161.
[16] D.A. Perkins, J.P. Attfield, J. Chem. Soc., Chem. Commun. (1991) 229.
[17] S.A. De Waal, E.A. Viljoen, L.C. Calk, Trans. Geol. Soc. S. Afr. 77 (1974) 373.
[18] M. Abe, K. Kaneta, M. Gomi, S. Nomura, J. Phys. Colloq. C2-40 (1979) 325.
[19] J.C. Fernandes, R.B. Guimarães, M.A. Continentino, H.A. Borges, A. Sulpice, J-L. Tholence, J.L. Siqueira, L.I. Zawislak, J.B.M. da Cunha, C.A. dos Santos, Phys. Rev. B58 (1998) 287.
[20] J-P. Morel, J. Phys. Chem. Solids 28 (1967) 629.
[21] J. Chappert, R.B. Frankel, Phys. Rev. Lett. 19 (1967) 570.
[22] A.H. Morrish, K. Haneda, J. Appl. Phys. 52 (1981) 2496.
[23] D. Kedem, T. Rothem, Phys. Rev. Lett. 18 (1987) 165.
[24] S. Mørup, E. Tronc, Phys Rev. Lett. 72 (1994) 3278.
[25] S. Boquet, R.J. Pollard, J.D. Cashion, Phys. Rev. B46 (1990) 11657.
[26] R. Wolfe, R.D. Pierce, M. Eibschutz, J.W. Nielsen, Solid State Commun. 7 (1967) 949.
[27] J.A. Sawicki, J. Nucl. Mater. 264 (1999) 169.
[28] C. Pan, B.G. Jones, A.J. Machiels, Nucl. Eng. Design 99 (1987) 317.
[29] Waterside Corrosion of Zirconium Alloys in Nuclear Power Plants, IAEA, Vienna, 1998, IAEA-TECDOC-996.
[30] J.M. Partezana, W.A. Byers, M.Y. Young, N.D. Williams, D.A. Kaminski, presented at The Robust Fuel Program WG1 Meeting, Tampa, Florida, February 27–28, 2001.
[31] T. Sato, M. Shimada, J. Am. Ceram. Soc. 68 (1985) 277.
[32] M. Yoshimura, T. Hiuga, A. Sōmiya, J. Am. Ceram. Soc. 69 (1986) 573.
[33] B. Cox, C. Wu, J. Nucl. Mater. 199 (1993) 272;
B. Cox, C. Wu, J. Nucl. Mater. 224 (1995) 169.
[34] B. Cox, J. Nucl. Mater. 249 (1997) 87.